SCIENCE CHINA
Information Sciences

• RESEARCH PAPER •

November 2023, Vol. 66 212207:1–212207:22
https://doi.org/10.1007/s11432-022-3735-5

UAV swarm formation reconfiguration control based on variable-stepsize MPC-APCMPIO algorithm

Jian LIAO[1†], Jun CHENG[2†], Bin XIN[3†], Delin LUO[4*], Lihui ZHENG[5], Yuhang KANG[2] & Shaolei ZHOU[6]

[1]*School of Physics and Electronic Information, Gannan Normal University, Ganzhou* 341000*, China;*
[2]*Shenzhen Institute of Advanced Technology, Chinese Academy of Sciences, Shenzhen* 518055*, China;*
[3]*School of Automation, Beijing Institute of Technology, Beijing* 100081*, China;*
[4]*School of Aerospace Engineering, Xiamen University, Xiamen* 361102*, China;*
[5]*School of Electronic Information, Northwest University of Technology, Xi'an* 710129*, China;*
[6]*School of Basic Science, Naval Aviation University of PLA, Yantai* 264001*, China*

Received 5 December 2022/Revised 28 January 2023/Accepted 7 March 2023/Published online 26 October 2023

Abstract For a complex operational environment, to actualize safe obstacle avoidance and collision avoidance, a swarm must be capable of autonomous formation reconfiguration. First, this paper introduces the basic pigeon-inspired optimization (PIO) algorithm, and establishes the unmanned aerial vehicle motion model and the virtual leader swarm formation control structure. Then, given the above knowledge, the basic error objective function of a UAV swarm, obstacle avoidance objective function, and collision avoidance objective function are devised based on the variable-stepsize model predictive control technique. Next, the adaptive perception Cauchy mutation PIO algorithm is proposed by introducing the Cauchy mutation operator, adaptive weight factor, and roulette wheel selection into the basic PIO. This algorithm is used to optimally solve the abovementioned swarm objective functions. Ultimately, a set of comparative simulations are performed to verify the effectiveness and reliability of the proposed algorithm.

Keywords unmanned aerial vehicle swarm, formation reconfiguration, variable-stepsize model predictive control (MPC), adaptive perception Cauchy mutation pigeon-inspired optimization (APCMPIO), obstacle avoidance

Citation Liao J, Cheng J, Xin B, et al. UAV swarm formation reconfiguration control based on variable-stepsize MPC-APCMPIO algorithm. Sci China Inf Sci, 2023, 66(11): 212207, https://doi.org/10.1007/s11432-022-3735-5

1 Introduction

Of late, unmanned aerial vehicle (UAV) swarms play an increasingly momentous role in various aspects of human life [1–5], e.g., forest firefighting [6], escaped criminal apprehension [7], communication [8], traffic monitoring [9], disaster management [10], automatic surveillance [11], package delivery [12], target tracking [13], smart farming [14], mapping unknown areas [15], and collaborative attack [16]. Compared with a single UAV, a UAV swarm can perform more complex tasks, expand a sensing range, increase system redundancy, strengthen system payloads, reduce human resources, and enhance task success rates [17–19]. To save energy, improve robustness, and enhance efficiency, a UAV swarm usually forms a certain formation configuration when performing tasks [20, 21]. Formation control is a vital field of study of UAV swarm coordinated control. It makes a group of homogeneous or heterogeneous UAVs actualize an anticipated formation configuration on the premise of maintaining communication, avoiding obstacles and collisions concurrently [22–24].

The formation control of a UAV swarm usually has three components: formation forming, formation maintenance, and formation reconfiguration. The first two components are relatively simple, and generally aim at the time-invariant formation configuration [25, 26]. However, generally, a UAV swarm cannot

* Corresponding author (email: luodelin1204@xmu.edu.cn)
† Liao J, Cheng J, and Xin B have the same contribution to this work.

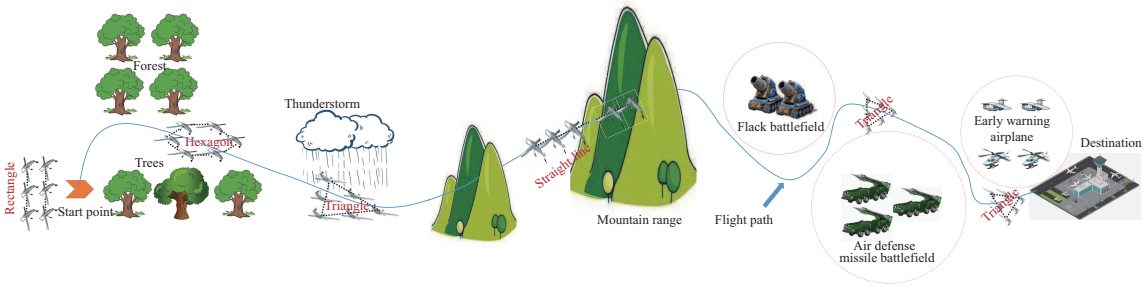

Figure 1 Formation reconfiguration of UAV swarm.

complete all tasks by only depending on a single formation configuration when it is confronted by a dynamic environment, transient situations, or sudden task instructions. In reality, a UAV swarm must have the ability of formation reconfiguration (Figure 1) [27,28]. In the formation reconfiguration process, a UAV swarm should not only heed maintaining communication, obstacle avoidance, or collision avoidance, as mentioned above, but also consider the constraints of the UAV itself and the limitations of the external environment [29, 30].

Inspired by the actual demand, researchers at home and abroad have paid extensive attention to the formation reconfiguration of UAV swarms. Chu et al. [31] used the piecewise approximation control parameter method to convert the energy-optimal leader follower formation reconfiguration issue of UAV swarms with terminal constraints into a convex optimization issue which is solved using open source software called CVX. Under undirected communication topology, Liao et al. [20] raised a new distributed cascade robust state feedback controller to solve the virtual leader formation and reconfiguration problem of a UAV swarm with control constraints and collision avoidance. On the basis of the concept of the precise penalty function mechanism, Liu et al. [32] proposed a new and improved hp-adaptive pseudospectral approach to tackle the leader follower formation reconfiguration problem of a UAV swarm with collision avoidance and communication constraints. By combining the gradient heuristic approach, Li et al. [33] developed a new hybrid offline optimization algorithm to address the leader follower formation reconfiguration problem of a UAV swarm with collision avoidance and communication constraints.

As can be seen from the aforementioned observation, the abovementioned formation reconfiguration control approaches are mostly developed based on the current state or output information, and these approaches cannot predict future information. However, formation reconfiguration is generally a control means taken by a UAV swarm in the face of some predicted or unexpected situations or events, and stability, rapidity, and accuracy are important performance indexes to measure the advantages and disadvantages of reconfiguration control approaches. To improve the performance of formation reconfiguration control approaches, researchers can combine some prediction approaches to develop a reconfiguration controller. Model predictive control (MPC), also known as receding horizon control, is effective and has been well verified in the research of UAV swarm formation control [34,35]. MPC, which is extensively applied in the field of formation control, is an excellent predictive control approach. For formation control problems with multiple constraints and strong coupling, MPC can convert them into optimal control problems in a finite time domain and solve them with rolling optimization [36]. On the basis of MPC, Zhang et al. [37] and Convens et al. [38] settled the formation forming control problem of a UAV swarm with collision avoidance. Liu et al. [39] used a fast MPC approach to settle the problems of UAV swarm virtual leader formation forming, maintenance, and obstacle avoidance. In terms of formation reconfiguration, Luis et al. [40] and Arul et al. [41] tackled the simple virtual leader formation reconfiguration problems of a UAV swarm with collision avoidance using a distributed MPC approach and a flatness-based MPC approach, respectively.

Although MPC can improve the robustness, stability, and accuracy of formation reconfiguration, its computational efficiency is not good because of the impact of the rolling optimization calculation, and it is often easy to fall into a locally optimal solution when solving the MPC algorithm. Since the bionic intelligent optimization algorithm came into being, it has been devoted to improving the computational efficiency and optimization effect. The pigeon-inspired optimization (PIO) algorithm is a typical representative of the bionic intelligent optimization algorithm which was first proposed by Duan et al. [42–45] in 2014 and has been widely applied to UAV swarm control. On the basis of graph theory knowledge, the PIO algorithm, and matrix analysis theory, Bai et al. [46] proposed a formation rapid forming approach

of UAV swarms with collision avoidance. To make a UAV swarm form a stable formation configuration quickly in an environment with obstacles, Qiu et al. [47] and Ruan et al. [48] developed distributed formation control approaches based on the multi-objective PIO algorithm. Combining the adaptive control technique and the PIO algorithm, Feng et al. [49] designed a rapid formation reconfiguration control approach for UAV swarms without obstacle avoidance.

Nevertheless, the current studies are mostly related to using the PIO algorithm to address the formation forming control problems of UAV swarms, while few studies have addressed formation reconfiguration control problems that are more meaningful. Even if such studies have been conducted, they do not involve a complex environment such as obstacles, which is primarily because the general PIO algorithm's ability to escape from a locally optimum solution is still limited. Motivated by the above facts and practical requirements, this study raises a novel distributed formation reconfiguration control approach based on variable-stepsize MPC-adaptive perception Cauchy mutation PIO (APCMPIO) algorithm. Compared with the previous achievements, the chief contributions of this paper are expounded below.

- Compared with [36–39,46–48], which merely studied the formation forming or maintenance problems of a UAV swarm with collision or obstacle avoidance, the virtual leader formation reconfiguration flight control of a UAV swarm in complex three dimensional (3D) environments (including 3D cylindrical and spherical obstacles) can be accomplished fast and stably in this study, and the proposed approach can satisfy the requirement of online computing (the runtime is less than the sampling period). Although Refs. [29–35, 40, 41, 48] investigated formation reconfiguration control problems, they did not involve obstacle avoidance, or only needed to avoid simple 3D cylindrical obstacles or two-dimensional (2D) circular obstacles.
- In contrast to [34–41], whose prediction time domain of the MPC approach was constant throughout the flight, this study proposes a novel variable-stepsize MPC approach, whose prediction time domain can switch between two values in accordance with whether the UAV swarm has discovered the obstacles. The proposed algorithm can make a tradeoff among the computational efficiency, the control accuracy, and the flight stability of a UAV swarm. Moreover, compared with the previous studies that used constant weight coefficients, this paper applies adaptive weight coefficients that are related to the obstacle parameters and the distance between UAVs and obstacles for the objective functions of various obstacles, so that the obstacle avoidance efficiency of a UAV swarm can be enhanced.
- In contrast to [42–44,46–49], which only applied the PIO algorithm with constant weight factor, this study's algorithm can diminish the probability of falling into locally optimal solution by introducing the Cauchy mutation into the PIO algorithm, to enhance the global optimization ability of the algorithm. In contrast to [45], whose Cauchy mutation condition is determined by judging whether the change value of recent iterations exceeds a certain threshold at two navigation phases, in this study, an adaptive global optimization and Cauchy mutation are conducted in accordance with the adaptive factor and roulette wheel/random principle at two navigation phases. In this way, they can control the speed of optimization and increase the diversity of the pigeon population on the premise of retaining excellent individuals. Additionally, the algorithm ensures the feasibility of the final output solution by recording the first feasible solution in the initialization phase.

The subsequent sections of this paper are shown as follows. Section 2 introduces the basic PIO algorithm and some basic knowledge of UAVs, including the UAV motion model and the swarm formation control structure. Section 3 presents the formation reconfiguration control problem of the UAV swarm under the framework of MPC. Section 4 presents the relevant knowledge of APCMPIO and raises the specific implementation steps that use the variable-stepsize MPC-APCMPIO algorithm to address the above reconfiguration control problem. Section 5 applies the comparative simulation case for illustration. Ultimately, Section 6 draws the conclusion.

2 Preliminary knowledge related to UAVs

This section reviews some preliminary knowledge, e.g., some common variables and notations (V/N) throughout this paper (Table 1), the PIO algorithm, the UAV motion model, and the swarm formation control structure.

Table 1 Variables and notations

V/N	Meaning	V/N	Meaning
$\mathbb{R}$	Set of real number	κ	A random value between $[0, 1]$
$N_{p1\max}$	Maximum iteration number during the first navigation	$N_{p2\max}$	Maximum iteration number during the second navigation
N	Number of isomorphic UAVs	β_v	Horizontal speed time constant
β_ψ	Yaw angle time constant	β_z	Altitude time constant
β_λ	Vertical speed time constant	$v_{\max}$	Upper bound of horizontal speed
$v_{\min}$	Lower bound of horizontal speed	$\psi_{\max}$	Upper bound of yaw angle
$\psi_{\min}$	Lower bound of yaw angle	$\lambda_{\max}$	Upper bound of vertical speed
$\lambda_{\min}$	Lower bound of vertical speed	$\Delta v_{\max}$	Upper bound of horizontal speed change rate
$\Delta\psi_{\max}$	Upper bound of yaw angle change rate	$\Delta\lambda_{\max}$	Upper bound of vertical speed change rate

2.1 Basic PIO algorithm

Pigeons can return to their nests by relying on three navigation tools: the sun, the geomagnetic field, and the conversant visual landmarks. Inspired by this feature, Duan et al. [47] developed the PIO algorithm for solving optimization problems. In the basic PIO algorithm, every pigeon's position symbolizes a potential optimization solution, and pigeons in the population need to utilize a map, compass, and landmark operator to navigate in two phases to find the global optimal solution. The above three navigation operators come from the sun, the geomagnetic field, and conversant visual landmarks in turn.

Supposing that there are $\tilde{N}$ pigeons in an M-dimensional space, the speed and position of the ith pigeon can be described as $\Theta_i = [\eta_{i1}, \eta_{i2}, \ldots, \eta_{iM}]^{\mathrm{T}} \in \mathbb{R}^M$ and $\Psi_i = [\xi_{i1}, \xi_{i2}, \ldots, \xi_{iM}]^{\mathrm{T}} \in \mathbb{R}^M$, respectively.

During the first navigation phase, the speed and position iteration formulas of the ith pigeon can be expressed as

$$\begin{cases} \Theta_i(N_t) = \Theta_i(N_t - 1) \times \mathrm{e}^{-S \times N_t} + \kappa \times (\Psi_{\mathrm{gbest}} - \Psi_i(N_t - 1)), \\ \Psi_i(N_t) = \Psi_i(N_t - 1) + \Theta_i(N_t), \qquad N_t = 1, 2, \ldots, N_{p1\max}, \end{cases} \tag{1}$$

where N_t, S, and $\Psi_{\mathrm{gbest}} \in \mathbb{R}^M$ symbolize the current iteration number, the map and compass factor, and the global best position of the pigeon during the $N_t - 1$ iteration, respectively. If the iteration number of the map operator and the compass operator attains the maximum iteration number $N_{p1_{\max}}$, the first navigation phase must be completed.

During the second navigation phase, the position iteration formulas of the ith pigeon can be expressed as

$$\begin{cases} \tilde{N}(N_t) = \left\lceil \dfrac{\tilde{N}(N_t - 1)}{2} \right\rceil, \\ \Psi_{\mathrm{center}}(N_t - 1) = \dfrac{\sum_{i=1}^{\tilde{N}(N_t - 1)} \Psi_i(N_t - 1) F(\Psi_i(N_t - 1))}{\sum_{i=1}^{\tilde{N}(N_t - 1)} F(\Psi_i(N_t - 1))}, \qquad N_t = 1, 2, \ldots, N_{p2\max}, \\ \Psi_i(N_t) = \Psi_i(N_t - 1) + \kappa \times (\Psi_{\mathrm{center}}(N_t - 1) - \Psi_i(N_t - 1)), \end{cases} \tag{2}$$

where $\lceil \cdot \rceil$ symbolizes the ceiling function, $\Psi_{\mathrm{center}}(N_t - 1) \in \mathbb{R}^M$ symbolizes the current weighted center position of the population after the $N_t - 1$ iteration, and $F(\Psi_i(N_t - 1)) \in \mathbb{R}$ symbolizes the fitness value of $\Psi_i(N_t - 1)$. If the iteration number of the landmark operator attains the maximum iteration number $N_{p2_{\max}}$, the second navigation phase must be completed and the optimization results can be acquired.

2.2 UAV motion model

Consider that a UAV swarm includes N isomorphic UAVs, and the motion model of UAV$_i$ in the swarm can be expressed as follows [47]:

$$\begin{cases} x_i(k+1) = x_i(k) + v_i(k)\tau(k)\sin\psi_i(k), \\ y_i(k+1) = y_i(k) + v_i(k)\tau(k)\cos\psi_i(k), \\ z_i(k+1) = z_i(k) + \lambda_i(k)\tau(k), \\ v_i(k+1) = v_i(k) + \dfrac{(v_i^c(k) - v_i(k))\tau(k)}{\beta_v}, \\ \psi_i(k+1) = \psi_i(k) + \dfrac{(\psi_i^c(k) - \psi_i(k))\tau(k)}{\beta_\psi}, \\ \lambda_i(k+1) = \lambda_i(k) + \dfrac{(z_i^c(k) - z_i(k))\tau(k)}{\beta_z} - \dfrac{\lambda_i(k)\tau(k)}{\beta_\lambda}, \end{cases} \quad i = 1, 2, \ldots, N, \tag{3}$$

where $x_i(k)$, $y_i(k)$, and $z_i(k)$ symbolize position coordinates of UAV$_i$ at $t = k$. $v_i(k)$, $\psi_i(k)$, and $\lambda_i(k)$ symbolize the horizontal speed, yaw angle, and vertical speed of UAV$_i$ at $t = k$, respectively. $v_i^c(k)$, $\psi_i^c(k)$, and $z_i^c(k)$ symbolize the horizontal speed control input, yaw angle control input, and altitude control input of UAV$_i$ at $t = k$, respectively. $\tau(k)$ symbolizes the sampling period. The yaw angle symbolizes the angle between the horizontal speed of a UAV and the OY axis in the geographic coordinate frame.

As noted from (3), the motion model of UAVs selected in this study is a semi-decoupled model, that is, the horizontal and vertical control inputs are independent of each other. Then, suppose that the state variables and control variables of UAV$_i$ at $t = k$ are expressed as follows:

$$\begin{aligned} X_i(k) &= [(X_i^{xy}(k))^{\mathrm{T}} \quad (X_i^z(k))^{\mathrm{T}}]^{\mathrm{T}} = [x_i(k) \quad y_i(k) \quad v_i(k) \quad \psi_i(k) \quad z_i(k) \quad \lambda_i(k)]^{\mathrm{T}} \in \mathbb{R}^6, \\ U_i(k) &= [(U_i^{xy}(k))^{\mathrm{T}} \quad (U_i^z(k))^{\mathrm{T}}]^{\mathrm{T}} = [v_i^c(k) \quad \psi_i^c(k) \quad z_i^c(k)]^{\mathrm{T}} \in \mathbb{R}^3, \end{aligned}$$

where

$$\begin{aligned} X_i^{xy}(k) &= [x_i(k) \quad y_i(k) \quad v_i(k) \quad \psi_i(k)]^{\mathrm{T}} \in \mathbb{R}^4, \\ X_i^z(k) &= [z_i(k) \quad \lambda_i(k)]^{\mathrm{T}} \in \mathbb{R}^2, \\ U_i^{xy}(k) &= [v_i^c(k) \quad \psi_i^c(k)]^{\mathrm{T}} \in \mathbb{R}^2, \\ U_i^z(k) &= [z_i^c(k)]^{\mathrm{T}} \in \mathbb{R}. \end{aligned}$$

Then Eq. (3) can be simplified to

$$X_i(k+1) = f(X_i(k), U_i(k)), \qquad i = 1, 2, \ldots, N, \tag{4}$$

and the relevant constraints of UAV are expressed as

$$\begin{cases} v_{\min} \leqslant v_i(k) \leqslant v_{\max}, \\ \psi_{\min} \leqslant \psi_i(k) \leqslant \psi_{\max}, \\ \lambda_{\min} \leqslant \lambda_i(k) \leqslant \lambda_{\max}, \\ \dfrac{|v_i(k+1) - v_i(k)|}{\tau(k)} \leqslant \Delta v_{\max}, \\ \dfrac{|\psi_i(k+1) - \psi_i(k)|}{\tau(k)} \leqslant \Delta \psi_{\max}, \\ \dfrac{|\lambda_i(k+1) - \lambda_i(k)|}{\tau(k)} \leqslant \Delta \lambda_{\max}. \end{cases} \tag{5}$$

2.3 Swarm formation control structure

Assumption 1. The swarm formation control structure is a virtual leader formation control structure which is shown in Figure 2 in this paper.

Assumption 2. There exists no time delay and packet loss when the virtual leader UAV transmits information with each UAV in this paper.

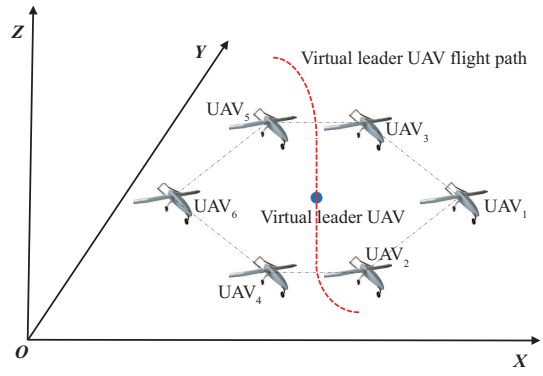

Figure 2 (Color online) Virtual leader formation control structure.

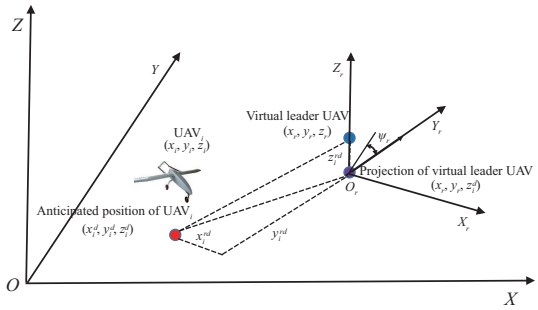

Figure 3 (Color online) Schematic diagram of distance angle formation.

Assumption 3. The motion model of the virtual leader UAV is identical to the above UAVs' motion models in this paper.

Considering that there exists a pre-planned flight path of the virtual leader UAV, all UAVs regard the virtual leader UAV as a reference, and maintain a certain distance and angle with it.

Suppose that the position coordinates, horizontal speed, yaw angle, and vertical speed of the virtual leader UAV are $(x_r(k), y_r(k), z_r(k))$, $v_r(k)$, $\psi_r(k)$ and $\lambda_r(k)$ at $t = k$, respectively. Additionally, the actual position coordinates, actual horizontal speed, actual yaw angle, actual vertical speed, anticipated position coordinates, anticipated horizontal speed, anticipated yaw angle, and anticipated vertical speed of UAV$_i$ are $(x_i(k), y_i(k), z_i(k))$, $v_i(k)$, $\psi_i(k)$, $\lambda_i(k)$, $(x_i^d(k), y_i^d(k), z_i^d(k))$, $v_i^d(k)$, $\psi_i^d(k)$, and $\lambda_i^d(k)$ at $t = k$, respectively. Then the 3D schematic of the distance angle formation can be acquired in Figure 3.

Figure 3 shows that $OXYZ$ and $O_rX_rY_rZ_r$ symbolize the geographic coordinate system and body coordinate frame of the virtual leader UAV, respectively. The OZ axis is parallel to the O_rZ_r axis. The blue, purple, and red solid circles and the physical UAV symbolize the position of the virtual leader UAV, the projection position of the virtual leader UAV on the OXY plane, the anticipated position of UAV$_i$, and the actual position of UAV$_i$, respectively. The horizontal speed of the virtual leader UAV is parallel to the O_rY_r axis. The relative distances between the anticipated position of UAV$_i$ and the virtual leader UAV in the $O_rX_rY_rZ_r$ coordinate system are $x_i^{rd}(k), y_i^{rd}(k)$, and $z_i^{rd}(k)$, respectively. Note that the abovementioned relative distances are the anticipated formation configuration that is pre-planned. On the basis of the semi-decoupled motion model of UAVs, the relationship between the anticipated position of UAV$_i$ and the position of the virtual leader UAV, the error of UAV$_i$, and the error variables on the OXY plane and the OZ axis can be described as follows:

$$\begin{bmatrix} x_i^d(k) \\ y_i^d(k) \\ z_i^d(k) \end{bmatrix} = \begin{bmatrix} x_r(k) \\ y_r(k) \\ z_r(k) \end{bmatrix} + \begin{bmatrix} \cos\psi_r(k) & \sin\psi_r(k) & 0 \\ -\sin\psi_r(k) & \cos\psi_r(k) & 0 \\ 0 & 0 & 1 \end{bmatrix} \cdot \begin{bmatrix} x_i^{rd}(k) \\ y_i^{rd}(k) \\ z_i^{rd}(k) \end{bmatrix}, \tag{6}$$

$$E_i^{xy}(k) = \begin{bmatrix} e_i^x(k) \\ e_i^y(k) \\ e_i^\psi(k) \end{bmatrix} = \begin{bmatrix} x_i(k) - x_i^d(k) \\ y_i(k) - y_i^d(k) \\ \psi_i(k) - \psi_i^d(k) \end{bmatrix}, \tag{7}$$

$$E_i^z(k) = \left[e_i^z(k) \right] = \left[z_i(k) - z_i^d(k) \right]. \tag{8}$$

3 Objective function design of the swarm formation configuration control problem based on MPC

3.1 Basic objective function design

The core idea of the MPC approach is that it can acquire the optimal control sequence of the controlled plant by optimizing the objective function in finite time, and the first data in the acquired control sequence

will be taken as the control input of the system at the current time. Its essence is to establish a finite time domain rolling optimization problem for all UAVs and solve it. Thus, inspired by the above analysis, the basic prediction model of UAV_i at $t = k$ can be acquired as follows:

$$X_i(k+s_p+1|k) = f(X_i(k+s_p|k), U_i(k+s_m|k)),\ s_p = 0,1,\ldots,N_p-1,\ s_m = 0,1,\ldots,N_m-1, \quad (9)$$

where N_p and N_m symbolize the prediction time domain and control time domain, $X_i(k+s_p|k)$ symbolizes the prediction made at $t = k$ about the states of UAV_i at $t = k+s_p$, $X_i(k|k) = X_i(k)$, and $U_i(k+s_m|k)$ symbolizes the prediction made at $t = k$ about the control inputs of UAV_i at $t = k+s_m$, $U_i(k|k) = U_i(k)$.

Based on the error and control input of UAV_i, the objective function can be defined as follows:

$$\begin{aligned} J_i^{xy}(X_i,U_i,k) = &\sum_{s_p=0}^{N_p-1}((E_i^{xy}(k+s_p|k))^{\mathrm{T}}Q_i^{xy}E_i^{xy}(k+s_p|k)) + \sum_{s_m=0}^{N_m-1}(U_i^{xy}(k+s_m|k))^{\mathrm{T}}R_i^{xy}U_i^{xy}(k+s_m|k)\\ &+ (E_i^{xy}(k+N_p|k))^{\mathrm{T}}Q_{N_p}^{xy}E_i^{xy}(k+N_p|k), \end{aligned} \quad (10)$$

$$\begin{aligned} J_i^{z}(X_i,U_i,k) = &\sum_{s_p=0}^{N_p-1}((E_i^{z}(k+s_p|k))^{\mathrm{T}}Q_i^{z}E_i^{z}(k+s_p|k)) + \sum_{s_m=0}^{N_m-1}(U_i^{z}(k+s_m|k))^{\mathrm{T}}R_i^{z}U_i^{z}(k+s_m|k)\\ &+ (E_i^{z}(k+N_p|k))^{\mathrm{T}}Q_{N_p}^{z}E_i^{z}(k+N_p|k), \end{aligned} \quad (11)$$

where $E_i^{xy}(k+s_p|k)$ and $E_i^{z}(k+s_p|k)$ symbolize the prediction made at $t = k$ about the error of UAV_i at $t = k+s_p$, respectively. $U_i^{xy}(k+s_p|k)$ and $U_i^{z}(k+s_p|k)$ symbolize the prediction made at $t = k$ about the control input of UAV_i at $t = k+s_m$, respectively. $Q_i^{xy} = (Q_i^{xy})^{\mathrm{T}} > 0, Q_i^{xy} \in \mathbb{R}^{3\times3}$, $Q_i^{z} > 0, Q_i^{z} \in \mathbb{R}$, $R_i^{xy} = (R_i^{xy})^{\mathrm{T}} > 0, R_i^{xy} \in \mathbb{R}^{3\times3}$, $R_i^{z} > 0, R_i^{z} \in \mathbb{R}$, $Q_{N_P}^{xy} = (Q_{N_P}^{xy})^{\mathrm{T}} > 0, Q_{N_P}^{xy} \in \mathbb{R}^{3\times3}$, and $Q_{N_P}^{z} > 0$, $Q_{N_P}^{z} \in \mathbb{R}$ are given weight matrices.

3.2 Obstacle avoidance objective function design

In military or civilian fields, a UAV swarm must traverse complex external environments to perform tasks [50, 51]. For instance, in package delivery in an urban environment, there will certainly be various obstacles such as buildings and trees; in an information-based battlefield, the swarm for long-range reconnaissance, attack, and damage assessment must avoid natural no fly zones such as thunderstorm areas, jungles, and mountains, as well as man-made military threats such as flack battlefields, air defense missile battlefields, and early warning airplanes. To safely and smoothly cross the above obstacles, threats, and no fly zones (as shown in Figure 1) and complete the tasks, an effective obstacle avoidance method should be developed for UAV swarms to operate in such environments. Current research mostly focuses on 2D plane space, and uses circles to represent the above obstacles, threats, and no fly zones. However, this paper focuses on the situation of three-dimensional geometric space. Obviously, circles in 2D plane space are not applicable. Most studies, such as [49], chose to regard obstacles, threats, and no fly zones as cylinders, but it may not always be appropriate. Given the above facts, this paper chooses to classify the above obstacles, threats, and no fly zones into three types of obstacles. Early warning airplanes are considered spheres (as shown in Figure 4), thunderstorm areas, buildings, trees, jungles, and mountains are considered cylinders with limited or unlimited height (as shown in Figure 5), and flack battlefields, and air defense missile battlefields are considered as hemisphere (as shown in Figure 6). Next, we will design the objective function for the above three types of obstacles under the MPC framework.

Assumption 4. The early warning airplane can cruise randomly in a small area that can be considered as a small sphere with a fixed center, and its detection distance is very large and remains unchanged. The center of the small sphere can be considered as the center of the spherical obstacle, and the sum of the radius of the small sphere and the detection distance of the early warning airplane can be considered as the radius of the spherical obstacle.

Figure 4 depicts the process of avoiding spherical obstacles. The red dotted line and the black dashed sphere surrounding UAV_i symbolize the flight path of UAV_i and the obstacle avoidance and UAV's collision avoidance protection area whose center point is the geometric center of UAV_i, respectively. The detection distance of UAVs, the radius of the UAV protection area, and the radius of the jth spherical obstacle are d^d, R^p, and R_j^s, respectively. Notably, $d^d > R^p + R_j^s$ and R^p of all UAVs are identical. The

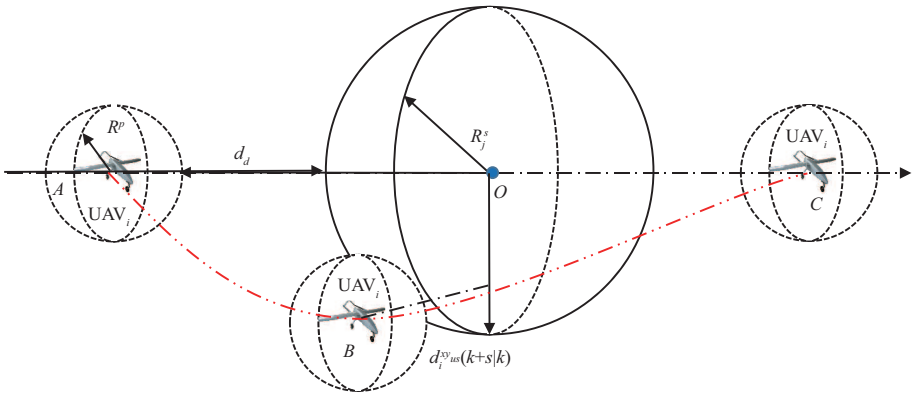

Figure 4 (Color online) UAV obstacle avoidance (spherical obstacle).

UAV can change its horizontal speed, yaw angle, and vertical speed to avoid the spherical obstacle when it discovers the spherical obstacle at point A (the spherical obstacle is within the detection distance at this time), and then passes through points B to C. Normally, suppose that the UAV will choose a flight path with the shortest range on the premise of ensuring safety and satisfying various constraints.

If the vertical distance between the center of the jth spherical obstacle and the flight speed direction of UAV$_i$ is greater than the sum of R_j^s and R^p, then UAV$_i$ can actualize safe obstacle avoidance. Otherwise, UAV$_i$ will collide with the jth spherical obstacle. Relying on the prediction idea of MPC, the state information at the current time and in the prediction time domain can be acquired by all UAVs. Once spherical obstacles appear within the detection range of UAVs, UAVs will conduct spherical obstacle avoidance prediction. If UAVs collide with spherical obstacles in the prediction time domain, a certain degree of punishment is required, otherwise, there is no punishment.

Suppose that there are N_s spherical obstacles. On the basis of the semi-decoupled motion model of UAVs, the objective functions of UAV$_i$ avoiding the jth spherical obstacle on the OXY plane and the OZ axis at $t=k$ are constructed as follows:

$$J_{ij}^{xy_s}(X_i,U_i,k)=\begin{cases}0, & d_i^{ss}(k)\geqslant R^p+R_j^s,\\ \sum\limits_{s_p=0}^{N_p} r_s^{xy}\dfrac{N_p-s_p}{d_i^{xy_{us}}(k+s_p|k)-R^p-R_j^{xy_s}}, & d_i^{ss}(k)<R^p+R_j^s,\end{cases}\tag{12}$$

$$J_{ij}^{z_s}(X_i,U_i,k)=\begin{cases}0, & d_i^{ss}(k)\geqslant R^p+R_j^s,\\ \sum\limits_{s_p=0}^{N_p} r_s^z(N_p-s_p)(z_i(k)+\Delta h-z_i(k+s_p|k))^2, & d_i^{ss}(k)<R^p+R_j^s,\end{cases}\tag{13}$$

$$d_i^{xy_{us}}(k+s_p|k)=((x_i(k+s_p|k)-x_j^s)^2+(y_i(k+s_p|k)-y_j^s)^2)^{1/2},$$

$$R_j^{xy_s}=((R_j^s)^2-(z_i(k)-z_j^s)^2)^{1/2},$$

$$r_s^{xy}=r^{xy}(d_i^{xy_{us}}(k+s_p|k)/R_j^{xy_s})^2,\quad r_s^z=r^z(\Delta h/0.1\Delta\lambda_{\max})^2,$$

$$d_i^{ss}(k)=\Gamma/(v_i^2(k)+\lambda_i^2(k))^{1/2},$$

$$\begin{aligned}\Gamma=&((\lambda_i(k)(y_i(k)-y_j^s)-v_i(k)\cos\psi_i(k)(z_i(k)-z_j^s))^2+(v_i(k)\sin\psi_i(k)(z_i(k)-z_j^s)\\&-\lambda_i(k)(x_i(k)-x_j^s))^2+(v_i(k)\cos\psi_i(k)(x_i(k)-x_j^s)-v_i(k)\sin\psi_i(k)(y_i(k)-y_j^s))^2)^{1/2},\end{aligned}$$

where $d_i^{xy_{us}}(k)=d_i^{xy_{us}}(k|k)$, (x_j^s,y_j^s,z_j^s) and $R_j^{xy_s}$ symbolize the position coordinates of jth spherical obstacle and the tangent circle radius of spherical obstacle at the height of $z_i(k)$, and r^{xy} and r^z symbolize basic weight factors for avoiding obstacles on the OXY plane and OZ axis. r_s^{xy} and r_s^z symbolize weight factors for avoiding spherical obstacles on the OXY plane and the OZ axis. Δh symbolizes the anticipated climbing height of each sampling period. $d_i^{xy_{us}}i(k+s_p|k)$ symbolizes the prediction made at $t=k$ about the distances on the OXY plane between UAV$_i$ and the center of the jth spherical obstacle at $t=k+s_p$,

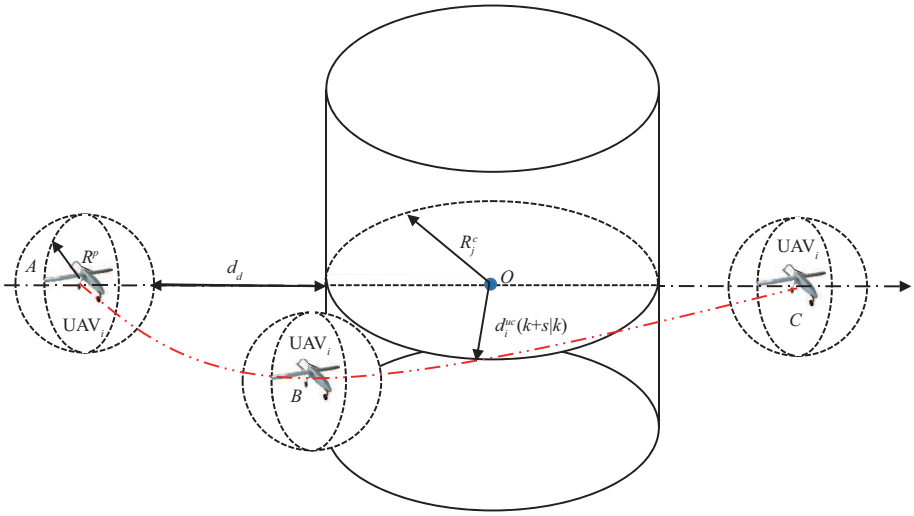

Figure 5 (Color online) UAV obstacle avoidance (cylindrical obstacle).

and $d_i^{ss}(k)$ symbolizes the vertical distance between the center of the jth spherical obstacle and the flight speed direction of UAV$_i$.

Figure 5 depicts the process of avoiding cylindrical obstacles. The radius and height of the jth cylindrical obstacle are R_j^c and h_j^c, respectively. If the flight altitude $z_i(k)$ of UAV$_i$ is larger than h_j^c, UAV$_i$ does not need to avoid the jth cylindrical obstacle. Suppose that there are N_c cylindrical obstacles. On the basis of the semi-decoupled motion model of UAV, the objective functions of UAV$_i$ avoiding the jth cylindrical obstacle on the OXY plane and the OZ axis at $t=k$ are constructed as follows:

$$J_{ij}^{xy_c}(X_i,U_i,k)=\begin{cases}0, & z_i(k)>h_j^c+R^p,\\ 0, & z_i(k)\leqslant h_j^c+R^p, d_i^{cs}(k)\geqslant R^p+R_j^c,\\ \sum\limits_{s_p=0}^{N_p} r_c^{xy}\dfrac{N_p-s_p}{d_i^{uc}(k+s_p|k)-R^p-R_j^c}, & z_i(k)\leqslant h_j^c+R^p, d_i^{cs}(k)<R^p+R_j^c,\end{cases} \tag{14}$$

$$J_{ij}^{z_c}(X_i,U_i,k)=\begin{cases}0, & z_i(k)>h_j^c+R^p,\\ \sum\limits_{s_p=0}^{N_p} r_c^z(N_p-s_p)(h_j^c+R^p-z_i(k+s_p|k))^2, & z_i(k)\leqslant h_j^c+R^p,\end{cases} \tag{15}$$

$$d_i^{uc}(k+s_p|k)=((x_i(k+s_p|k)-x_j^c)^2+(y_i(k+s_p|k)-y_j^c)^2)^{1/2},$$

$$r_c^{xy}=r^{xy}(d_i^{uc}(k+s_p|k)/R_j^c)^2,\quad r_c^z=r^z((h_j^c+R^p)/z_i(k))^2,$$

$$d_i^{cs}(k)=\begin{cases}|(x_i(k)-x_j^c)\cot\psi_i(k)-(y_i(k)-y_j^c)|/(1+(\cot\psi_i(k))^2)^{1/2}, & \psi_i(k)\neq 0,\\ |(x_i(k)-x_j^c)|, & \psi_i(k)=0,\end{cases}$$

where $d_i^{uc}(k)=d_i^{uc}(k|k)$, (x_j^c,y_j^c,z_j^c), r_c^{xy}, and r_c^z symbolize the position coordinates of the jth cylindrical obstacle, and the weight factor for avoiding cylindrical obstacles on the OXY plane and the OZ axis, respectively. $d_i^{uc}(k+s_p|k)$ symbolizes the prediction made at $t=k$ of the distances between UAV$_i$ and the center of the jth cylindrical obstacle at $t=k+s_p$, and $d_i^{cs}(k)$ symbolizes the vertical distance between the center of the jth cylindrical obstacle and the flight speed direction of UAV$_i$.

Suppose that the heights of some cylindrical obstacles (thunderstorm areas) are infinite, while other cylindrical obstacle heights (buildings, trees, jungles, and mountains) are finite in this paper. If a UAV swarm detects the former type of cylindrical obstacle, it will choose to bypass the obstacle on the OXY plane. If the latter type of obstacle is detected, it will determine the obstacle avoidance mode by comparing the distance of leaping over the obstacle on the OZ axis with the distance of bypassing the obstacle

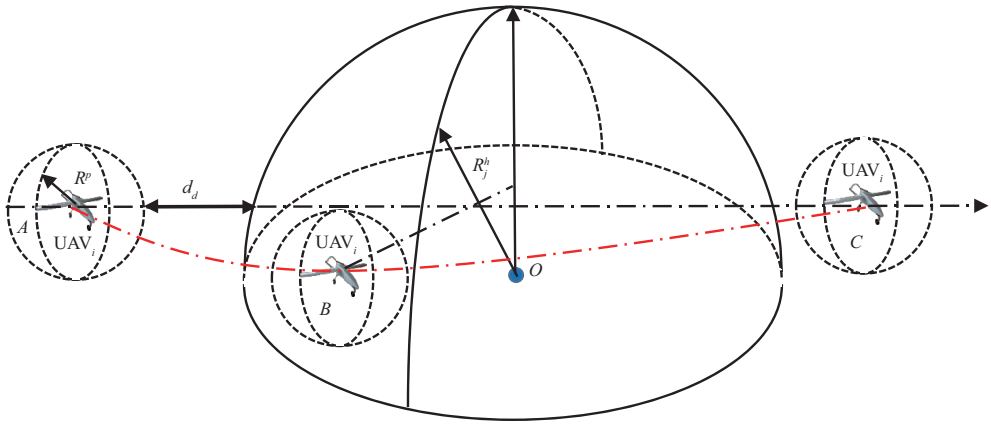

Figure 6 (Color online) UAV obstacle avoidance (hemispherical obstacle).

on the OXY plane.

$$J_{ij}^{xyz_c}(X_i,U_i,k)=\begin{cases}J_{ij}^{xy_c}, & h_j^c=+\infty,\\ J_{ij}^{z_c}, & h_j^c<+\infty,\ d_i^t(k)<d_i^a(k),\\ J_{ij}^{xy_c}, & h_j^c<+\infty,\ d_i^t(k)>d_i^a(k),\end{cases} \tag{16}$$

$$d_i^t(k)=2R_j^c+2((h_j^c-z_i(k))^2+(((x_i(k)-x_j^c)^2+(y_i(k)-y_j^h)^2)^{1/2}-R_j^c)^2)^{1/2},$$

$$d_i^a(k)=\pi R_j^c+2(((x_i(k)-x_j^c)^2+(y_i(k)-y_j^c)^2)^{1/2}-R_j^c),$$

where $d_i^t(k)$ and $d_i^a(k)$ symbolize the distances of leaping over cylindrical obstacles on the Z axis and bypassing cylindrical obstacles on the OXY plane, respectively.

Figure 6 depicts the process of avoiding hemispherical obstacles. The radius of the jth hemispherical obstacle is R_j^h. The approach of hemispherical obstacle avoidance is similar to that of spherical obstacle avoidance. Suppose that there are N_h hemispherical obstacles. On the basis of the semi-decoupled motion model of UAVs, the objective functions of UAV$_i$ avoiding the jth hemispherical obstacle on the OXY plane and the OZ axis at $t=k$ are constructed as follows:

$$J_{ij}^{xy_h}(X_i,U_i,k)=\begin{cases}0, & z_n(k)<z_j^h,\\ 0, & z_n(k)>z_j^h, d_i^{hs}(k)\geqslant R^p+R_j^h,\\ \sum\limits_{s_p=0}^{N_p} r_h^{xy}\dfrac{N_p-s_p}{d_i^{xy_{uh}}(k+s_p|k)-R^p-R_j^{xy_h}}, & z_n(k)>z_j^h, d_i^{hs}(k)<R^p+R_j^h,\end{cases} \tag{17}$$

$$J_{ij}^{z_h}(X_i,U_i,k)=\begin{cases}0, & z_n(k)<z_j^h,\\ 0, & z_n(k)>z_j^h, d_i^{hs}(k)\geqslant R^p+R_j^h,\\ \sum\limits_{s_p=0}^{N_p} r_h^z(N_p-s_p)(z_i(k)+\Delta h-z_i(k+s_p|k))^2, & z_n(k)>z_j^h, d_i^{hs}(k)<R^p+R_j^h,\end{cases} \tag{18}$$

$$d_i^{xy_{uh}}(k+s_p|k)=((x_i(k+s_p|k)-x_j^h)^2+(y_i(k+s_p|k)-y_j^h)^2)^{1/2},$$

$$R_j^{xy_h}=((R_j^h)^2-(z_i(k)-z_j^h)^2)^{1/2},$$

$$r_h^{xy}=r^{xy}\left(\frac{d_i^{xy_{uh}}(k+s_p|k)}{R_j^{xy_h}}\right)^2,\quad r_h^z=r^z(\Delta h/0.1\Delta\lambda_{\max})^2,$$

$$z_n(k)=\frac{((x_i(k)-x_j^h)v_i(k)\sin\psi_i(k)+(y_i(k)-y_j^h)v_i(k)\cos\psi_i(k)+(z_i(k)-z_j^h)\lambda_i(k))\lambda_i(k)}{v_i^2(k)+\lambda_i^2(k)},$$

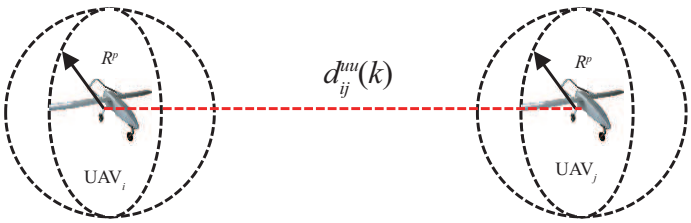

Figure 7 (Color online) UAV collision avoidance.

$$d_i^{hs}(k) = \frac{\Lambda}{(v_i^2(k) + \lambda_i^2(k))^{1/2}},$$

$$\Lambda = ((\lambda_i(k)(y_i(k) - y_j^h) - v_i(k)\cos\psi_i(k)(z_i(k) - z_j^h))^2 + (v_i(k)\sin\psi_i(k)(z_i(k) - z_j^h) - \lambda_i(k)(x_i(k) - x_j^h))^2 + (v_i(k)\cos\psi_i(k)(x_i(k) - x_j^h) - v_i(k)\sin\psi_i(k)(y_i(k) - y_j^h))^2)^{1/2},$$

where $d_i^{xy_{uh}}(k) = d_i^{xy_{uh}}(k|k)$, (x_j^h, y_j^h, z_j^h) and $R_j^{xy_h}$ symbolize the position coordinates of the jth hemispherical obstacle and the tangent circle radius of the hemispherical obstacle at the height of $z_i(k)$. r_h^{xy} and r_h^z symbolize the position coordinates of the jth hemispherical obstacle, and the weight factor for avoiding hemispherical obstacles on the OXY plane and the OZ axis, respectively. $d_i^{xy_{uh}}(k + s_p|k)$ symbolizes the prediction made at $t = k$ about the distances on the OXY plane between UAV$_i$ and the center of the jth hemispherical obstacle at $t = k + s_p$, $d_i^{hs}(k)$ symbolizes the vertical distance between the center of the jth hemispherical obstacle and the flight speed direction of UAV$_i$. $z_n(k)$ symbolizes the perpendicular point coordinate from the center of the jth hemispherical obstacle to the flight speed direction.

3.3 Collision avoidance objective function design

Assumption 5. There exists no time delay and packet loss in the information transmission among UAVs in this paper.

Because of the requirement of changing positions during swarm formation reconfiguration, particularly in short-range reconnaissance, collision avoidance among UAVs is also one of the key points that need important attention [52–55]. Based on the aforementioned collision avoidance protection area of UAVs, for each UAV, this study considers other UAVs as moving obstacles and proposes priority rules, so that the internal collision avoidance problem of a UAV swarm can be transformed into an obstacle avoidance problem of moving obstacles.

Limited by its relevant constraints, a UAV cannot change its state instantly. Nevertheless, in this paper, the current states of UAVs and the predicted states in the prediction time domain can be acquired by applying MPC, and then the distances between UAVs at the current time and in the prediction domain time can be calculated. Accordingly, we can predict whether UAVs will collide and reduce the collision probability. If the distance between UAV$_i$ and UAV$_j$ is greater than $2{\cdot}R^p$ at the current time and in the prediction domain time, the collision risk temporarily does not need to be considered. Conversely, the risk needs (as shown in Figure 7).

Without loss of generality, a compromise is made among the safety of UAVs, collision avoidance efficiency, and the error between actual states and anticipated states of UAVs. Given this fact, this paper proposes the priority rules of UAVs which are as follows:

(1) The priority of the UAV that needs to avoid obstacles is higher. If several UAVs need to avoid obstacles, the type of obstacles should be considered; the higher the degree of an obstacle threat is, the higher the priority of the UAV is. According to the degree of the obstacle threat, sphere obstacles > hemisphere obstacles > cylindrical obstacles.

(2) A UAV closer to the virtual leader UAV has a higher priority.

(3) The priority of the UAV that is closer to the anticipated position is higher.

(4) Among the above priorities, priority 1 > priority 2 > priority 3.

If one UAV collides with another UAV within the predicted domain time, the UAV with lower priority must be punished. At this time, the UAV with higher priority flies in accordance with the previously planned trajectory. Meanwhile, the UAV with lower priority changes its state to actualize safe collision avoidance. The specific collision avoidance process is shown in Figure 8.

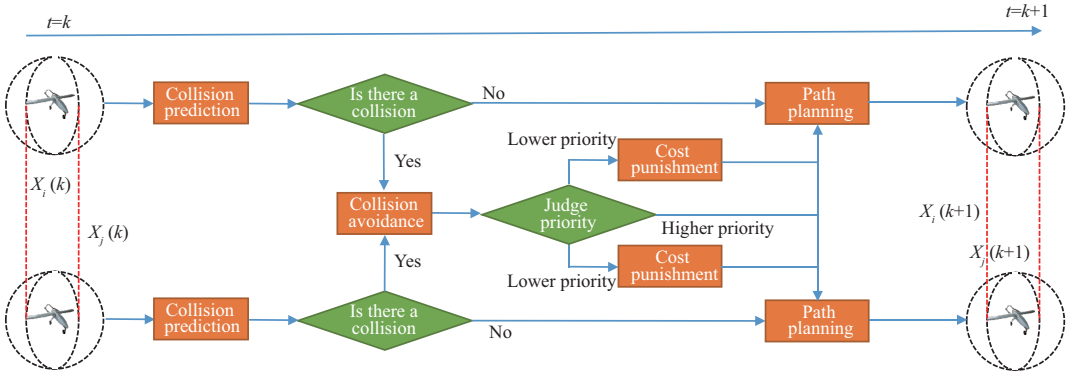

Figure 8 (Color online) Flow-process diagram of UAV collision avoidance.

On the basis of the semi-decoupled motion model of UAVs, the objective functions of UAV$_i$ avoiding UAV$_j$ on the OXY plane and the OZ axis at $t = k$ are constructed as follows:

$$J_{ij}^{xy_{uu}}(X_i, U_i, k) = \begin{cases} 0, & p_i > p_j, \\ 0, & p_i < p_j, d_{ij}^{uu}(k) > 2R^p, \\ \sum\limits_{s_p=0}^{N_p} r_u^{xy} \dfrac{N_p - s_p}{d_{ij}^{xy_{uu}}(k+s_p|k)}, & p_i < p_j, d_{ij}^{uu}(k) < 2R^p, \end{cases} \tag{19}$$

$$J_{ij}^{z_{uu}}(X_i, U_i, k) = \begin{cases} 0, & p_i > p_j, \\ 0, & p_i < p_j, d_{ij}^{uu}(k) > 2R^p, \\ \sum\limits_{s_p=0}^{N_p} r_u^{z} \dfrac{N_p - s_p}{d_{ij}^{z_{uu}}(k+s_p|k)}, & p_i < p_j, d_{ij}^{uu}(k) < 2R^p, \end{cases} \tag{20}$$

$$d_{ij}^{uu}(k) = ((x_i(k) - x_j(k))^2 + (y_i(k) - y_j(k))^2 + (z_i(k) - z_j(k))^2)^{1/2},$$

$$d_{ij}^{xy_{uu}}(k+s_p|k) = ((x_i(k+s_p|k) - x_j(k+s_p|k))^2 + (y_i(k+s_p|k) - y_j(k+s_p|k))^2)^{1/2},$$

$$d_{ij}^{z_{uu}}(k+s_p|k) = |z_i(k+s_p|k) - z_j(k+s_p|k)|,$$

where $d_{ij}^{xy_{uu}}(k) = d_{ij}^{xy_{uu}}(k|k)$, $d_{ij}^{z_{uu}}(k) = d_{ij}^{z_{uu}}(k|k)$, and r_s symbolize the weight factor for avoiding collisions. $d_{ij}^{uu}(k+s_p|k)$, $d_{ij}^{xy_{uu}}(k+s_p|k)$, and $d_{ij}^{z_{uu}}(k+s_p|k)$ symbolize the prediction made at $t = k$ about the distance, the distance on the OXY plane, and the distance on the OZ axis between UAV$_i$ and UAV$_j$ at $t = k + s_p$. p_i and p_j symbolizes the priority of UAV$_i$ and UAV$_j$, respectively. r_u^{xy} and r_u^z symbolize weight factors for avoiding collisions on the OXY plane and the OZ axis, respectively.

Therefore, on the basis of the semi-decoupled motion model of UAVs, the objective functions of UAV$_i$ at $t = k$ on the OXY plane and the OZ axis at $t = k$ can be summarized as follows:

$$J_{\text{total}_i}^{xy^*} = \arg\min_{J_{\text{total}_i}^{xy}} \left\{ J_i^{xy} + \sum_{j=1}^{N_s} J_{ij}^{xy_s} + \sum_{j=1}^{N_c} J_{ij}^{xyz_c} + \sum_{j=1}^{N_h} J_{ij}^{xy_h} + \sum_{j=1, i\neq j}^{N} J_{ij}^{xy_{uu}} \right\}, \tag{21}$$

$$J_{\text{total}_i}^{z^*} = \arg\min_{J_{\text{total}_i}^{z}} \left\{ J_i^{z} + \sum_{j=1}^{N_s} J_{ij}^{z_s} + \sum_{j=1}^{N_c} J_{ij}^{xyz_c} + \sum_{j=1}^{N_h} J_{ij}^{z_h} + \sum_{j=1, i\neq j}^{N} J_{ij}^{z_{uu}} \right\}, \tag{22}$$

$$\text{s.t.}\begin{cases} X_i(k+s_p+1|k) = f(X_i(k+s_p|k), U_i(k+s_p|k)), \\ v_{\min} \leqslant v_i(k) \leqslant v_{\max}, \\ \psi_{\min} \leqslant \psi_i(k) \leqslant \psi_{\max}, \\ \lambda_{\min} \leqslant \lambda_i(k) \leqslant \lambda_{\max}, \\ \dfrac{|v_i(k+1)-v_i(k)|}{\tau(k)} \leqslant \Delta v_{\max}, \\ \dfrac{|\psi_i(k+1)-\psi_i(k)|}{\tau(k)} \leqslant \Delta \psi_{\max}, \\ \dfrac{|\lambda_i(k+1)-\lambda_i(k)|}{\tau(k)} \leqslant \Delta \lambda_{\max}. \end{cases}$$

Remarkably, the previous research work on employing MPC to address the formation control problems of UAV swarms mostly used a constant prediction time domain. However, considering the environment amidst the winds of change faced by UAV swarms, particularly in future information-based military battlefields, the public ordinarily hopes that UAV swarms can predict as much as possible what will happen in the future before obstacles are detected. Thus the prediction time domain should be longer at this phase. Conversely, to reduce calculation and improve the control accuracy and response speed as much as possible, the prediction time domain should be shorter after obstacles are detected. Given the above factors, this study designs a prediction time domain selective switcher as follows:

$$N_p = \begin{cases} N_{p\_l}, & \text{if there are no obstacles within detection distance,} \\ N_{p\_s}, & \text{otherwise,} \end{cases} \tag{23}$$

where N_{p_l} and N_{p_s} symbolize long and short prediction time domains, respectively.

4 Controller design based on improved MPC-APCMPIO

4.1 Relevant knowledge of APCMPIO

Bionic intelligent optimization algorithms have the dilemma of falling into locally optimal solutions, particularly in a complex search space, such as the search space in the process of swarm reconfiguration. To solve this dilemma, scholars have tried to make various improvements, such as to the PIO algorithm. By studying the multi-control surfaces control approach of large civil aircraft, Duan et al. [45] found that the probability of falling into a locally optimal solution can be substantially abated on the premise of guaranteeing the calculation efficiency of the algorithm by introducing Cauchy mutation terms into three PIO operators. Motivated by these research results, this paper proposes an intelligent optimization algorithm APCMPIO, and uses it to optimize the swarm reconfiguration problem.

In the first navigation phase of APCMPIO, introducing the adaptive weight factor into the speed iteration formula of the ith pigeon, Eq. (24) can be obtained as

$$\Theta_i(N_t) = \Theta_i(N_t-1) \times \mathrm{e}^{-S\times N_t} + \kappa \times \omega_i(N_t) \times (\Psi_{\text{gbest}} - \Psi_i(N_t-1)), \tag{24}$$

where $\omega_i(N_t)$ symbolizes the adaptive weight factor, which can be obtained using

$$\omega_i(N_t) = \begin{cases} \omega_{\min} + (\omega_{\max}-\omega_{\min}) \times \dfrac{F(\Psi_{ij}(N_t)) - F_{\min}(N_t)}{F_{\text{average}}(N_t) - F_{\min}(N_t)}, & F(\Psi_{ij}(N_t)) \leqslant F_{\text{average}}(N_t), \\ \omega_{\max}, & F(\Psi_{ij}(N_t)) > F_{\text{average}}(N_t), \end{cases} \tag{25}$$

where $\omega_{\min}$ and $\omega_{\max}$ symbolize the minimum and maximum weight factor, respectively. $F_{\text{average}}(N_t)$ and $F_{\min}(N_t)$ are the average and the minimum fitness values after N_t iterations, respectively. Generally, the smaller the fitness value after N_t iterations is, the closer the optimal solution is, and local search is more necessary. In contrast, the larger the fitness value is, the farther the optimal solution is, and a global search is more necessary.

The density function of the Cauchy distribution can be defined as follows:

$$f(\eta) = \frac{1}{\pi}\frac{p}{p^2+\xi^2}, \qquad \xi \in (-\infty, +\infty), \tag{26}$$

where $\pi = 3.14$ symbolizes circumference ratio, and p symbolizes a density function parameter.

Given the definition of the Cauchy distribution probability density function, the following equation can be acquired:

$$\int_{-\infty}^{\Psi_i - \Psi_{\text{gbest}}} \frac{1}{\pi} \frac{p}{p^2 + \xi^2} \mathrm{d}\xi = \frac{1}{\pi} \arctan\xi \Big|_{-\infty}^{\Psi_i - \Psi_{\text{gbest}}} = \kappa. \tag{27}$$

In the first navigation phase of APCMPIO, first, determine the number of pigeons that must be mutated in accordance with a certain probability p_m. This is $\tilde{N} \times p_m$. Then select $\tilde{N} \times p_m$ pigeons based on the roulette wheel principle, and their position iteration formulas will be obtained by conducting a Cauchy mutation operation. Based on (27), the following equation can be obtained:

$$\Psi_i = \Psi_{\text{gbest}} + p\tan\Big(\pi\Big(\kappa - \frac{1}{2}\Big)\Big). \tag{28}$$

Consequently, if the ith pigeon must mutate, then Eq. (1) is transformed into

$$\begin{cases} \Theta_i(N_t) = \Theta_i(N_t - 1) \times \mathrm{e}^{-S \times N_t} + \kappa \times \omega_i(N_t) \times (\Psi_{\text{gbest}} - \Psi_i(N_t - 1)), \\ \Psi_i(N_t) = \Psi_i(N_t - 1) + \Theta_i(N_t) + p \times \tan\Big(\pi\Big(\kappa - \dfrac{1}{2}\Big)\Big), \quad N_t = 1, 2, \ldots, N_{p1\max}. \end{cases} \tag{29}$$

Otherwise, Eq. (1) is transformed into

$$\begin{cases} \Theta_i(N_t) = \Theta_i(N_t - 1) \times \mathrm{e}^{-S \times N_t} + \kappa \times \omega_i(N_t) \times (\Psi_{\text{gbest}} - \Psi_i(N_t - 1)), \\ \Psi_i(N_t) = \Psi_i(N_t - 1) + \Theta_i(N_t), \quad N_t = 1, 2, \ldots, N_{p1\max}. \end{cases} \tag{30}$$

In the second navigation phase of APCMPIO, first, select half of the pigeons as the parent pigeon population in accordance with the fitness value and calculate its center; then determine the number of pigeons that must be mutated in accordance with a certain probability p_m, that is $\tilde{N} \times p_m$. Next, select $\tilde{N} \times p_m$ pigeons based on random principle and conduct a Cauchy mutation operation in accordance with (31), while other pigeons will be transformed in accordance with (2), and these pigeons are considered as the child pigeon population. Mix the parent pigeon population with the child pigeon population as a new pigeon population, and select half of the pigeons in accordance with the fitness value as the next generation of the pigeon population.

$$\begin{cases} \tilde{N}(N_t) = \left\lceil \dfrac{\tilde{N}(N_t - 1)}{2} \right\rceil, \\ \Psi_{\text{center}}(N_t - 1) = \dfrac{\sum_{i=1}^{\tilde{N}(N_t - 1)} \Psi_i(N_t - 1) F(\Psi_i(N_t - 1))}{\sum_{i=1}^{\tilde{N}(N_t - 1)} F(\Psi_i(N_t - 1))}, \quad N_t = 1, 2, \ldots, N_{p2\max}, \\ \Psi_i(N_t) = \Psi_i(N_t - 1) + \kappa \times \Big(\Psi_{\text{center}}(N_t - 1) - \Psi_i(N_t - 1) + p\tan\Big(\pi\Big(\kappa - \dfrac{1}{2}\Big)\Big)\Big). \end{cases} \tag{31}$$

4.2 Description of controller design steps

During each step of variable-stepsize MPC, the anticipated state of the UAV swarm at the current time and the future time, the actual state of the UAV swarm at the current time, and the control input of the UAV swarm acquired in the previous step are applied to predict the actual state of the UAV swarm at a future time. Meanwhile, on the basis of the semi-decoupled motion model of UAV, the total objective functions of the swarm on the OXY plane and the OZ axis are acquired, respectively. Note that the total objective functions of the swarm on the OXY plane and the OZ axis are independent, and in accordance with the above two total objective functions, the horizontal control input on the OXY plane and vertical control input on the OZ axis can be optimized by APCMPIO. The calculation flow of the UAV swarm formation reconfiguration control approach is as follows:

(1) Set basic parameters of variable-stepsize MPC and APCMPIO.

(2) Initialize all pigeons in the pigeon flock algorithm, and record the first feasible solution that conforms to collision avoidance and obstacle avoidance conditions, and its corresponding control input.

(3) Calculate the positions of all pigeons in accordance with the total objective functions of the swarm on the OXY plane and the OZ axis.

Table 2 Initial states of UAVs

UAV	x (m)	y (m)	z (m)	v (m/s)	ψ (°)	λ (m/s)
UAV1	16	110	6	8	95	0
UAV2	16	125	8	7	96	0
UAV3	16	100	10	8	98	0
UAV4	4	125	10	6	95	0
UAV5	4	100	8	12	96	0
UAV6	4	110	6	10	98	0
Virtual leader	10	110	20	10	100	0

(4) Start the first navigation phase, and conduct an iterative calculation on the speeds and positions of all pigeons in the pigeon flock in accordance with (29) and (30).

(5) Start the second navigation phase, and conduct an iterative calculation on the position of all pigeons in the pigeon flock in accordance with (2) and (31).

(6) After the above two navigation phases, verify the optimal solution of the output to determine whether it satisfies the constraint conditions. If it is satisfied, then the final global best position Ψ_{gbest} is considered as the control input $U_i(k|k)$ of the UAV swarm at $t = k$; otherwise, the control input corresponding to recorded feasible solution before the optimization algorithm starts running is considered as the control input $U_i(k|k)$ of the UAV swarm at $t = k$.

5 Simulation

This section provides a UAV swarm formation reconfiguration case, in consideration of formation transformation, leaping over/bypassing mountains and forests, avoiding threat areas such as air defense missile battlefields and early warning airplanes, and bypassing no-fly zones such as thunderstorm areas, to verify the effectiveness and reliability of the algorithm in this paper. The PIO algorithm in [42], CMPIO algorithm in [45], and particle swarm optimization (PSO) algorithm in [56] are used as comparative studies in this case. Notably, the parameters of the UAV motion model, constraints, initial states of UAVs, and flight trajectory of the virtual leader applied in the proposed and comparative algorithms are identical.

Consider a UAV swarm containing six UAVs (fixed wing or rotor wing) that must perform one task of long-distance transportation of materials, as shown in Figure 1. The starting point of the UAV swarm is symbolized by the red arrow, the destination point is an airport for storing materials, and there are various natural barriers (such as thunderstorm areas, jungles, and mountains) and man-made military threats (such as flack battlefields, air defense missile battlefields, and early warning airplanes) lying between the starting and destination points. To perform this task smoothly and safely, the UAV swarm must avoid the above obstacles. UAVs have sufficient detection capability, and they adopt the virtual leader formation control structure. If obstacle types, quantities, positions, and other parameters are known in advance through reconnaissance, a safe and feasible flight trajectory can be devised for the virtual leader on the basis of the above information.

Suppose that the simulation time of the entire process is 100 s, and the sampling frequency is 2 Hz. The initial states of the six UAVs and the virtual leader UAV are shown in Table 2, the flight trajectory of the virtual leader is shown in Table 3, the formation shape of the UAV swarm is shown in Table 4, the UAV constraints are shown in Table 5, the obstacle parameters are shown in Table 6, the model parameters of UAVs, obstacle avoidance, and collision avoidance are shown in Table 7, and the parameters of MPC, PIO, PSO, CMPIO, and APCMPIO are shown in Table 8.

Figures 9–11 show the vertical view, sectional view, and 3D panorama view of UAV swarm formation reconfiguration trajectory during $t \in [0, 100]$ s by employing this paper's algorithm, respectively. The flight trajectories of the virtual leader UAV and six UAVs are symbolized by gray dashed line, and purple, cyan, blue, red, green, and magenta solid lines, respectively. The six UAVs are symbolized by purple, cyan, blue, red, green, and magenta-filled triangle. The formation configuration of the UAV swarm at $t = 0$ s, $t = 6$ s, $t = 12$ s, $t = 18$ s, $t = 24$ s, $t = 30$ s, $t = 36$ s, $t = 42$ s, $t = 48$ s, $t = 54$ s, $t = 60$ s, $t = 66$ s, $t = 72$ s, $t = 78$ s, $t = 84$ s, $t = 90$ s, $t = 96$ s and $t = 100$ s are connected by black dashed lines.

Figures 12–14 show the vertical speed, horizontal speed, and yaw angle change curves during $t \in [0, 100]$ s obtained by employing this paper's algorithm, respectively. Meanwhile, Figures 15–17 show the vertical speed, horizontal speed, and yaw angle change rate curves, respectively. Figure 18 shows the prediction

Table 3 Flight trajectory of the virtual leader UAV

Time interval (s)	v (m/s)	ψ/s (°/s)	λ (m/s)
[0, 24)	10	−0.0833	0
[24, 47)	10	−0.3019	0
[47, 50.5)	10	−0.3019	4
[50.5, 65.5)	10	−2.5352	0
[65.5, 69)	10	−2.5352	−4
[69, 82.5)	10	−2.5352	0
[82.5, 86)	10	−2.5352	−4
[86, 100]	10	−1.0714	0

Table 4 Formation shape of the UAV swarm

Time interval/shape	$(x_1^{rd}, y_1^{rd}, z_1^{rd})$	$(x_2^{rd}, y_2^{rd}, z_2^{rd})$	$(x_3^{rd}, y_3^{rd}, z_3^{rd})$	$(x_4^{rd}, y_4^{rd}, z_4^{rd})$	$(x_5^{rd}, y_5^{rd}, z_5^{rd})$	$(x_6^{rd}, y_6^{rd}, z_6^{rd})$
[0 s, 15 s)/hexagon	$(15, 0, 0)$ m	$(7.5, 13, 4)$ m	$(-7.5, 13, 4)$ m	$(7.5, -13, -4)$ m	$(-7.5, -13, -4)$ m	$(-15, 0, 0)$ m
[15 s, 100 s]/triangle	$(15, 0, 0)$ m	$(3.75, 6.5, 4)$ m	$(-3.75, 6.5, 4)$ m	$(7.5, -13, -4)$ m	$(-7.5, -13, -4)$ m	$(-7.5, 0, 0)$ m

Table 5 UAV constraints

Constraint variable	Minimum value	Maximum value
v (m/s)	5	15
ψ (°/s)	0	360
λ (m/s)	−5	5
Δv (m/s^2)	−4	4
$\Delta\psi$ (°/s^2)	−10	10
$\Delta\lambda$ (m/s^2)	−4	4

Table 6 Obstacle parameters

Obstacle	Obstacle type	x (m)	y (m)	z (m)	Radius (m)	Height (m)
The 1st cylindrical obstacle	Jungles area	28	115	–	44	6
The 2nd cylindrical obstacle	Jungles area	148	46	–	31	10
The 3rd cylindrical obstacle	Thunderstorm area	337	113	–	41	$+\infty$
The 4th cylindrical obstacle	Thunderstorm area	350	28	–	23	$+\infty$
The 5th cylindrical obstacle	Mountain area	475	250	–	48	32
The 6th cylindrical obstacle	Mountain area	615	60	–	45	30
The 1st hemispherical obstacle	Air defense area	565	160	0	90	–
The 1st spherical obstacle	Early warning area	695	305	63	60	–

Table 7 Model parameters of UAVs, obstacle avoidance, and collision avoidance

Variable	Value	Variable	Value
β_v (s)	1	β_z (s)	1
β_ψ (s)	0.75	β_λ (s)	0.3
r^{xy} (m)	15	r^z (m)	0.1
r_u^{xy} (m)	10	r_u^z (m)	20
Δh (m/s)	0.48	$\Delta\lambda_{\max}$ (m/s)	4
R^p (m)	2	d^d (m)	105

time domain switching value of the six UAVs. Figure 19 shows the error of the change curves between the actual position coordinates and the anticipated position coordinates of the six UAVs. Figure 20 shows the runtime of six UAVs when applying the APCMPIO algorithm (the results are acquired by calculating the average runtime of 20 simulations under identical conditions), and the maximum value, minimum value, and average value of the six UAVs' runtime are shown in Table 9. In Figures 12–17, 19, and 20, the curves of the six UAVs are symbolized by six different colors. Figure 21 shows the average runtime of different algorithms (the results are acquired by calculating the average runtime of 20 simulations under identical conditions), and each curve symbolizes the average runtime of the six UAVs (PSO algorithm [56], PIO algorithm [42], CMPIO algorithm [45] and APCMPIO algorithm). Figure 22 shows the total objective function change curves; the total objective function value is equal to the sum of the objective function

Table 8 Parameters of MPC, PIO, PSO, CMPIO, and APCMPIO

Parameter	Meaning	Value	Algorithm
N_{p_l}	Long prediction time domain	6	MPC
N_{p_s}	Short prediction time domain	3	MPC
N_m	Control time domain	3	MPC
Q_i^{xy}	Weight matrices	diag[0.1, 0.1, 15]	MPC
Q_i^z	Weight matrix	0.1	MPC
Q_{Np}^{xy}	Weight matrix	diag[0.1, 0.1, 15]	MPC
Q_{Np}^z	Weight matrix	0.1	MPC
R_i^{xy}	Weight matrices	diag[0.001, 0.001]	MPC
R_i^z	Weight matrices	0.001	MPC
$\tilde{N}$	Population size	50	PIO, PSO, CMPIO, APCMPIO
N_c	Iteration number	60	PSO
r_{PSO}	Weight factor	1	PSO
c_1	Acceleration factor	1.5	PSO
c_2	Acceleration factor	1.5	PSO
$N_{p1\max}$	Iteration number of first phase	50	PIO, CMPIO, APCMPIO
$N_{p2\max}$	Iteration number of second phase	10	PIO, CMPIO, APCMPIO
S	Map and compass factor	0.02	CMPIO, APCMPIO
p	Density function parameter	1	CMPIO, APCMPIO
N_{p_1}	Map and compass mutation condition	3	CMPIO
N_{p_2}	Landmark operator mutation condition	2	CMPIO
α_1	Map and compass mutation threshold	2	CMPIO
α_2	Landmark operator mutation threshold	0.02	CMPIO
p_m	mutation probability	0.06	APCMPIO
$\omega_{\min}$	Minimum weight factor	1	APCMPIO
$\omega_{\max}$	Maximum weight factor	1.5	APCMPIO

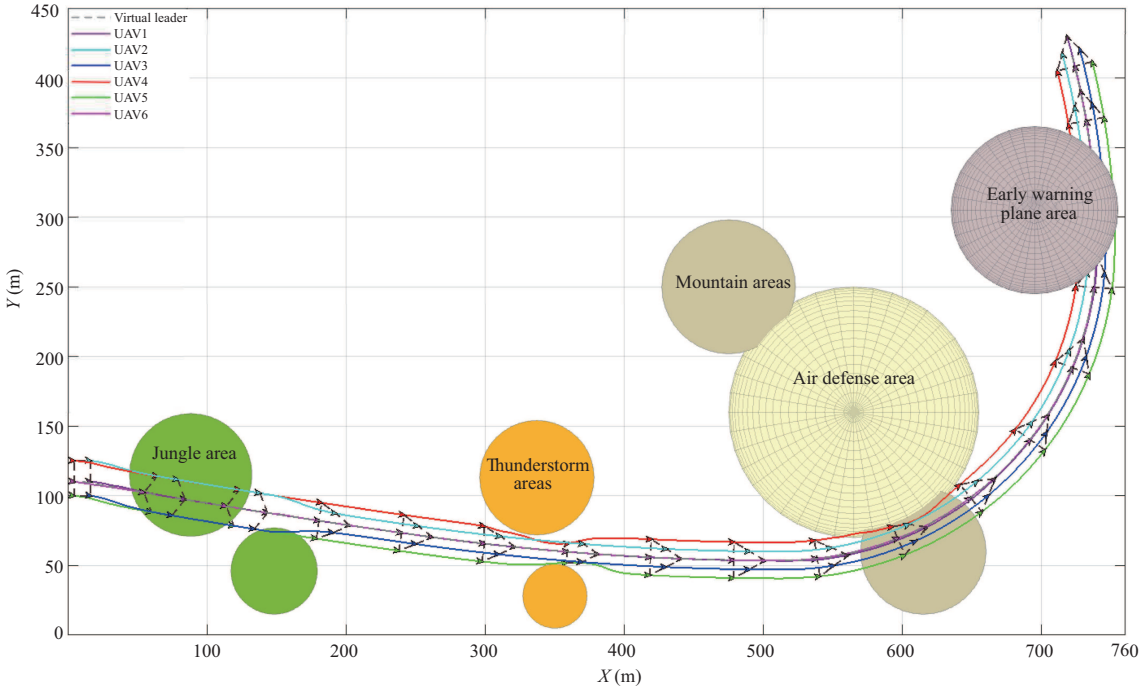

Figure 9 (Color online) Vertical view of the UAV swarm formation reconfiguration trajectories.

value on the OXY plane and the objective function on the OZ axis. The curves of four colors symbolize the total objective function values acquired by the PSO algorithm [56], PIO algorithm [42], CMPIO algorithm [45], and APCMPIO algorithm. Here, note that the value range of the yaw angle is limited to $[0°, 360°]$, but to make the yaw angle change curve more straightforward, the yaw angle is directly taken

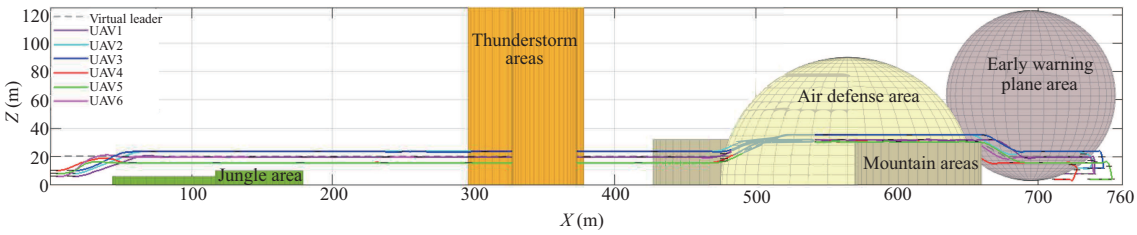

Figure 10 (Color online) Sectional view of the UAV swarm formation reconfiguration trajectories.

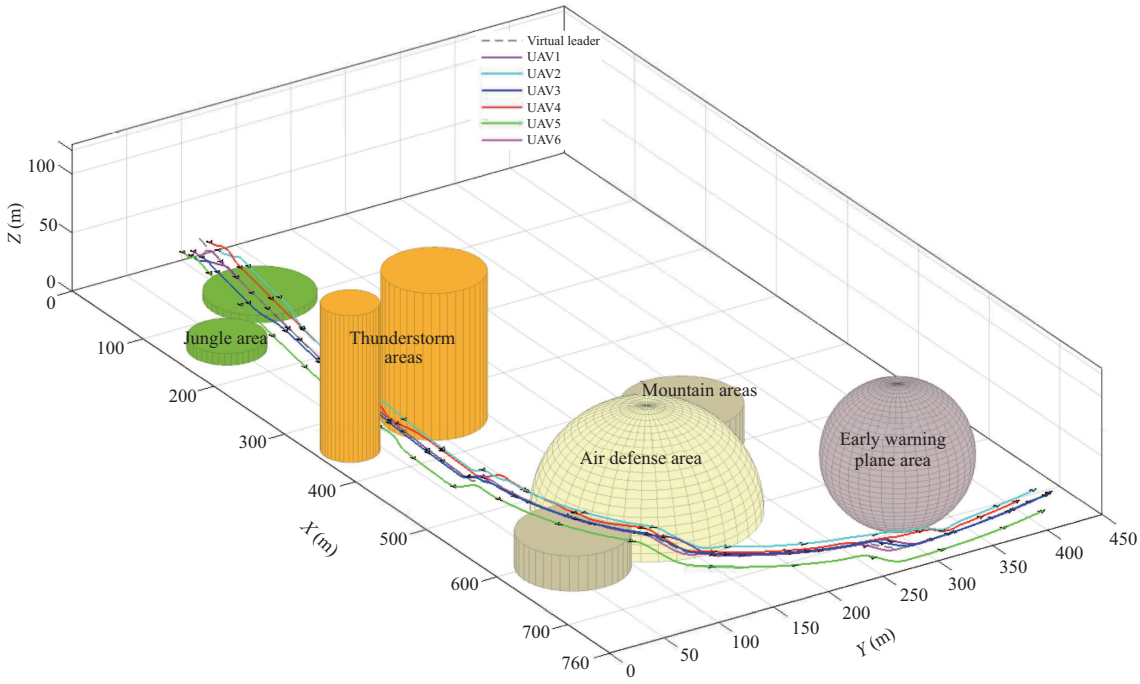

Figure 11 (Color online) 3D panorama view of the UAV swarm formation reconfiguration trajectories.

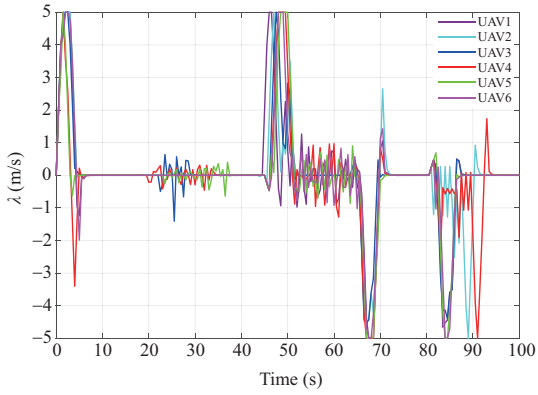

Figure 12 (Color online) Vertical speed change curves.

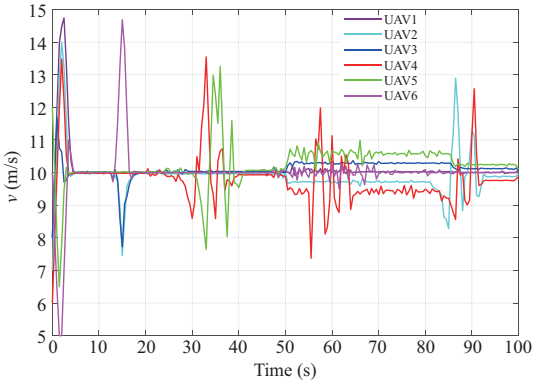

Figure 13 (Color online) Horizontal speed change curves.

as a negative value in this paper when it continues to decrease from 0°.

Figure 9 shows the initial configuration of the UAV swarm is a rectangle at $t = 0$ s, and there are just simple obstacles such as jungle areas in the initial phase of swarm flight. The command center presets an anticipated formation configuration of hexagon, and the swarm can quickly form this configuration at $t = 6$ s. Next, the environment will become complicated. When $t = 15$ s, the triangle becomes the anticipated formation configuration, it will change the formation again, and it can form that configuration at $t = 18$ s. Before encountering the thunderstorm areas, it can always maintain a triangle formation

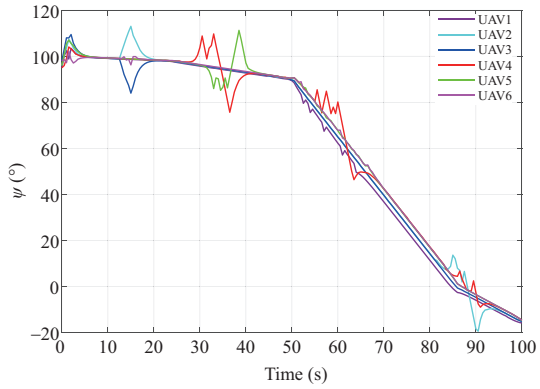

Figure 14 (Color online) Yaw angle change curves.

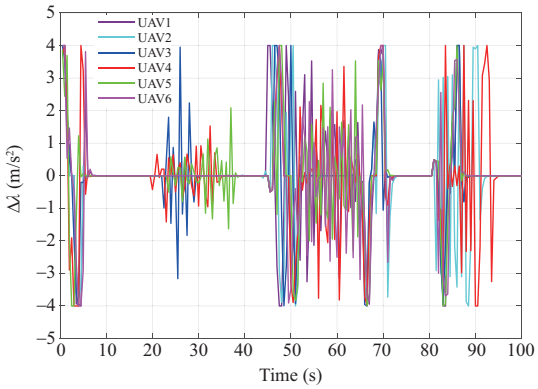

Figure 15 (Color online) Vertical speed change rate curves.

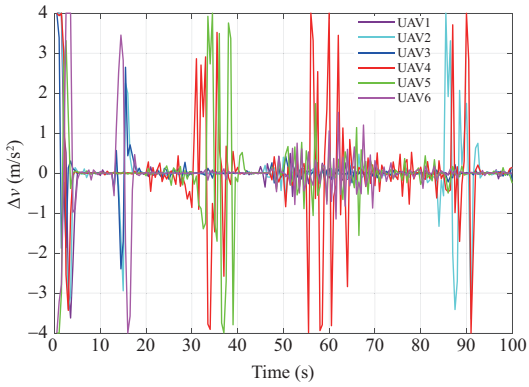

Figure 16 (Color online) Horizontal speed change rate curves.

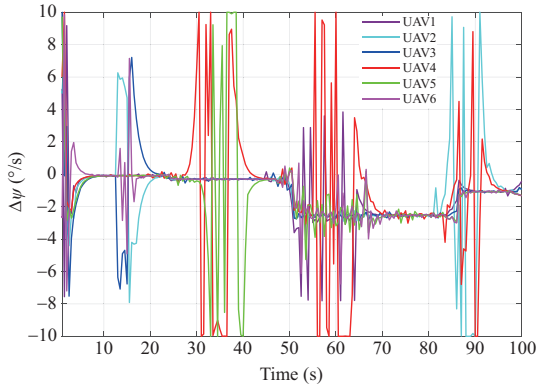

Figure 17 (Color online) Yaw angle change rate curves.

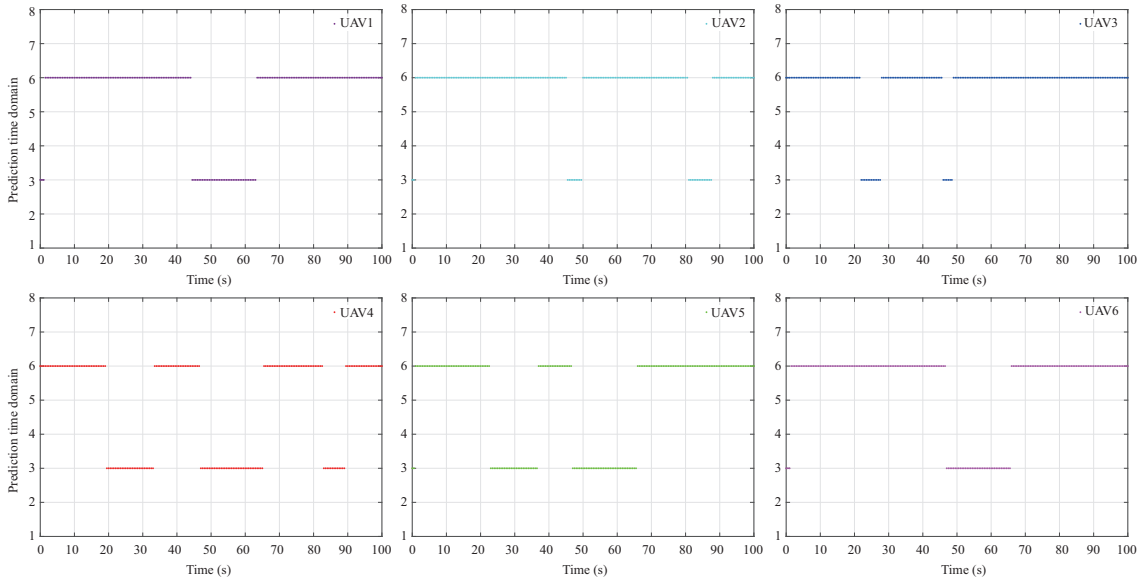

Figure 18 (Color online) Prediction time domain switching curves.

configuration. However, when thunderstorm obstacles appear, it needs to avoid these obstacles and cannot maintain the anticipated triangle formation configuration at $t = 36$ s because of the narrow space gap between two thunderstorm areas. Once it passes through the thunderstorm areas, it will reform the anticipated formation at $t = 42$ s. When encountering air defense areas, mountain areas or early warning

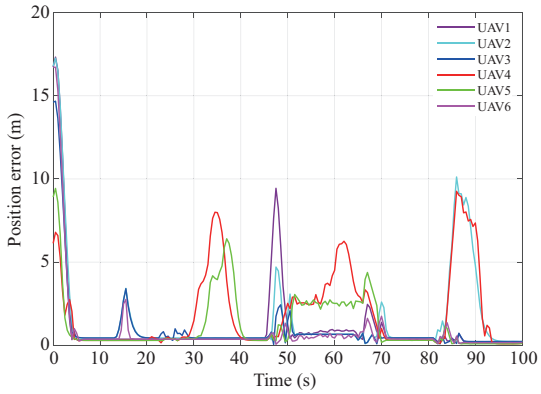

Figure 19 (Color online) Position error change curves.

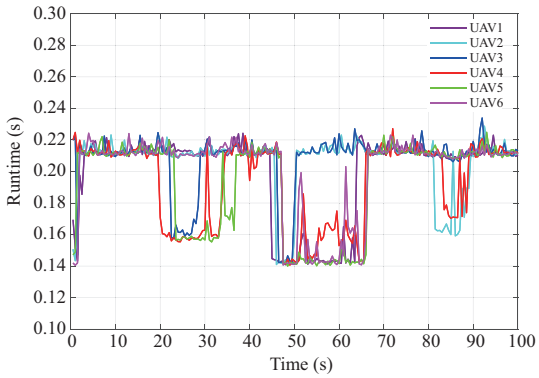

Figure 20 (Color online) Runtime of six UAVs.

Table 9 Maximum, minimum, and average values of six UAVs' runtime (s)

	UAV1	UAV2	UAV3	UAV4	UAV5	UAV6
Maximum value	0.2242	0.2287	0.2339	0.2271	0.2248	0.2242
Minimum value	0.1413	0.1410	0.1409	0.1406	0.1400	0.1405
Average value	0.1991	0.2062	0.2074	0.1928	0.1920	0.2002

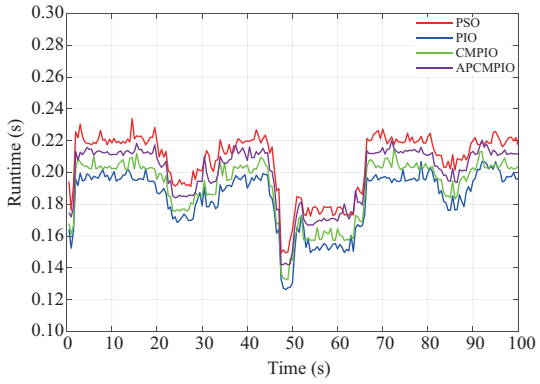

Figure 21 (Color online) Average runtime of different algorithms.

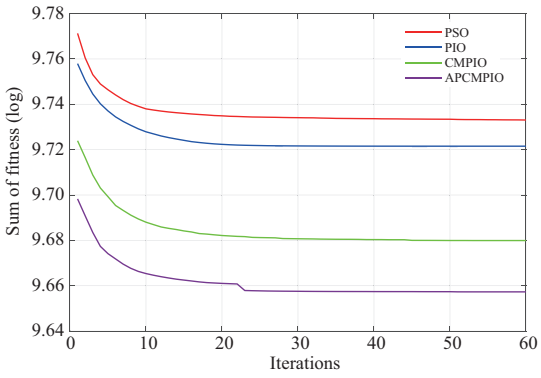

Figure 22 (Color online) Total objective function change curves.

areas appear in the subsequent flight phase; it can also smoothly avoid these obstacles and actualize formation reconfiguration.

Figure 10 shows the swarm avoids obstacles such as jungle areas and mountain areas by climbing in height. When encountering thunderstorm areas, it can only bypass these obstacles because they are too high. When encountering the air defense area, it can vertically climb over the area and laterally bypass it simultaneously. When encountering the early warning area, it can reduce the height and laterally bypass the area concurrently. Figure 11 further illustrates these facts in Figures 9 and 10.

Figures 12–14, and 19 show UAVs of different positions can take different manners to avoid these obstacles once they are encounter, and all the change values of vertical speed, horizontal speed, and yaw angle are within the range of the constraint conditions. When encountering these obstacles, the error of the six UAVs between the actual position coordinate and the anticipated position coordinate will appear, but once they cross these obstacles, the error will converge to zero. Meanwhile, Figures 14–16 show the values of the yaw angle change rate, vertical speed change rate, and horizontal speed change rate are within the range of constraint conditions as well. Figure 18 shows the prediction time domain of UAVs can be switched to the short prediction time domain $N_{p\_s} = 3$ when encountering obstacles; otherwise, it can be switched to the long prediction time domain $N_{p\_l} = 6$. Figure 20 and Table 9 show that when the APCMPIO algorithm is applied, the runtimes of the six UAVs are less than 0.24 s, while the sampling period adopted in this paper is 0.5 s. Then, we can judge that the algorithm proposed in our paper is

suitable for online applications. Figures 21 and 22 show that the algorithm proposed in this paper has good computational performance and the best convergence performance.

It can be concluded from the above facts that the proposed algorithm in this study can make the UAV swarm actualize formation reconfiguration in the face of a complex terrain environment, and compared with the algorithms in [42, 45, 56], the convergence speed of this paper's algorithm is faster.

6 Conclusion

This study proposes a variable-stepsize MPC-APCMPIO algorithm based on the virtual leader formation control structure of the distance angle to address the UAV swarm formation reconfiguration control problem in the face of a complex terrain environment. At the outset, a type of semi-decoupled UAV motion model whose control inputs on the OXY plane and the OZ axis are independent is adopted, and then several objective functions for various obstacles are devised on the basis of this motion model and the variable-stepsize MPC approach. Furthermore, an improved PIO algorithm is proposed for optimizing the above objective functions, and the validity and feasibility of this algorithm are verified by numerical simulation. In the future, we will extend this study by considering factors such as time delay, communication information package loss, and dynamic obstacles.

Acknowledgements This work was supported in part by National Natural Science Foundation of China (Grant No. 61973327), National Outstanding Youth Talents Support Program (Grant No. 61822304), Shanghai Municipal Science and Technology Major Project (Grant No. 2021SHZDZX0100), Shanghai Municipal Commission of Science and Technology Project (Grant No. 19511132101), Projects of Major International (Regional) Joint Research Program of NSFC (Grant No. 61720106011), and Science and Technology Research Project of Jiangxi Provincial Department of Education (Grant No. GJJ201410).

References

1 Huo M Z, Duan H B, Yang Q, et al. Live-fly experimentation for pigeon-inspired obstacle avoidance of quadrotor unmanned aerial vehicles. Sci China Inf Sci, 2019, 62: 052201
2 Tai J J, Phang S K, Wong F Y M. COAA* — an optimized obstacle avoidance and navigational algorithm for UAVs operating in partially observable 2D environments. Un Sys, 2022, 10: 159–174
3 Alladi T, Naren, Bansal G, et al. SecAuthUAV: a novel authentication scheme for UAV-ground station and UAV-UAV communication. IEEE Trans Veh Technol, 2020, 69: 15068–15077
4 Kim S K, Ahn C K, Shi P. Performance recovery tracking-controller for quadcopters via invariant dynamic surface approach. IEEE Trans Ind Inf, 2019, 15: 5235–5243
5 Wang X K, Shen L C, Liu Z H, et al. Coordinated flight control of miniature fixed-wing UAV swarms: methods and experiments. Sci China Inf Sci, 2019, 62: 212204
6 Harikumar K, Senthilnath J, Sundaram S. Multi-UAV Oxyrrhis marina-inspired search and dynamic formation control for forest firefighting. IEEE Trans Automat Sci Eng, 2019, 16: 863–873
7 Zheng Y J, Du Y C, Ling H F, et al. Evolutionary collaborative human-UAV search for escaped criminals. IEEE Trans Evol Computat, 2020, 24: 217–231
8 Yao K L, Xu Y H, Li H, et al. Leveraging partially overlapping channels for intra- and inter-coalition communication in cooperative UAV swarms. Sci China Inf Sci, 2021, 64: 140305
9 Oubbati O S, Atiquzzaman M, Lorenz P, et al. Search: an SDN-enabled approach for vehicle path-planning. IEEE Trans Veh Technol, 2020, 69: 14523–14536
10 Aiello G, Hopps F, Santisi D, et al. The employment of unmanned aerial vehicles for analyzing and mitigating disaster risks in industrial sites. IEEE Trans Eng Manage, 2020, 67: 519–530
11 Kim H, Ben-Othman J. A collision-free surveillance system using smart UAVs in multi domain IoT. IEEE Commun Lett, 2018, 22: 2587–2590
12 Sawadsitang S, Niyato D, Tan P S, et al. Joint ground and aerial package delivery services: a stochastic optimization approach. IEEE Trans Intell Transp Syst, 2019, 20: 2241–2254
13 Das A, Shirazipourazad S, Hay D, et al. Tracking of multiple targets using optimal number of UAVs. IEEE Trans Aerosp Electron Syst, 2019, 55: 1769–1784
14 Maddikunta P K R, Hakak S, Alazab M, et al. Unmanned aerial vehicles in smart agriculture: applications, requirements, and challenges. IEEE Sens J, 2021, 21: 17608–17619
15 Qin H L, Meng Z H, Meng W, et al. Autonomous exploration and mapping system using heterogeneous UAVs and UGVs in GPS-denied environments. IEEE Trans Veh Technol, 2019, 68: 1339–1350
16 Hu J Q, Wu H S, Zhan R J, et al. Self-organized search-attack mission planning for UAV swarm based on wolf pack hunting behavior. J Syst Eng Electron, 2021, 32: 1463–1476
17 Guo K X, Li X X, Xie L H. Simultaneous cooperative relative localization and distributed formation control for multiple UAVs. Sci China Inf Sci, 2020, 63: 119201
18 Hu J W, Wang M, Zhao C H, et al. Formation control and collision avoidance for multi-UAV systems based on Voronoi partition. Sci China Technol Sci, 2020, 63: 65–72
19 Liu C, Wang M, Zeng Q, et al. Leader-following flocking for unmanned aerial vehicle swarm with distributed topology control. Sci China Inf Sci, 2020, 63: 140312
20 Liao F, Teo R, Wang J L, et al. Distributed formation and reconfiguration control of VTOL UAVs. IEEE Trans Contr Syst Technol, 2017, 25: 270–277
21 Wang Y, Wang D B. Tight formation control of multiple unmanned aerial vehicles through an adaptive control method. Sci China Inf Sci, 2017, 60: 070207

22 Dong X W, Li Y F, Lu C, et al. Time-varying formation tracking for UAV swarm systems with switching directed topologies. IEEE Trans Neural Netw Learn Syst, 2019, 30: 3674–3685
23 Tran V P, Santoso F, Garratt M A, et al. Distributed formation control using fuzzy self-tuning of strictly negative imaginary consensus controllers in aerial robotics. IEEE ASME Trans Mechatron, 2021, 26: 2306–2315
24 Wang Y Z, Yue Y F, Shan M, et al. Formation reconstruction and trajectory replanning for multi-UAV patrol. IEEE ASME Trans Mechatron, 2021, 26: 719–729
25 Zhang L, Lu Y, Xu S D, et al. Multiple UAVs cooperative formation forming control based on back-stepping-like approach. J System Eng Electron, 2018, 29: 816–822
26 Wang Y, Cheng Z S, Xiao M. UAVs' formation keeping control based on multi-agent system consensus. IEEE Access, 2020, 8: 49000–49012
27 Wang X H, Zhang Y, Wang L Z, et al. Robustness evaluation method for unmanned aerial vehicle swarms based on complex network theory. Chin J Aeronautics, 2020, 33: 352–364
28 Kamel M A, Yu X, Zhang Y M. Formation control and coordination of multiple unmanned ground vehicles in normal and faulty situations: a review. Annu Rev Control, 2020, 49: 128–144
29 Mirzaeinia A, Hassanalian M, Lee K, et al. Energy conservation of V-shaped swarming fixed-wing drones through position reconfiguration. Aerospace Sci Tech, 2019, 94: 105398
30 Wubben J, Fabra F, Calafate C T, et al. A novel resilient and reconfigurable swarm management scheme. Comput Networks, 2021, 194: 108119
31 Chu J, Zhou Z, Guo J. Optimal reconfiguration of formation flying using a direct sequential method. IFAC-PapersOnLine, 2017, 50: 9398–9404
32 Liu G Q, Li B, Ji Y D. A modified HP-adaptive pseudospectral method for multi-UAV formation reconfiguration. ISA Trans, 2022, 129: 217–229
33 Li B, Zhang J W, Li D, et al. A hybrid offline optimization method for reconfiguration of multi-UAV formations. IEEE Trans Aerosp Electron Syst, 2021, 57: 506–520
34 Huang D P, Li H Y, Li X. Formation of generic UAVs-USVs system under distributed model predictive control scheme. IEEE Trans Circuits Syst II, 2020, 67: 3123–3127
35 Hafez A T, Marasco A J, Givigi S N, et al. Solving multi-UAV dynamic encirclement via model predictive control. IEEE Trans Contr Syst Technol, 2015, 23: 2251–2265
36 Cai Z H, Wang L H, Zhao J, et al. Virtual target guidance-based distributed model predictive control for formation control of multiple UAVs. Chin J Aeronautics, 2020, 33: 1037–1056
37 Zhang K W, Shi Y, Sheng H Y. Robust nonlinear model predictive control based visual servoing of quadrotor UAVs. IEEE ASME Trans Mechatron, 2021, 26: 700–708
38 Convens B, Merckaert K, Nicotra M M, et al. Safe, fast, and efficient distributed receding horizon constrained control of aerial robot swarms. IEEE Robot Autom Lett, 2022, 7: 4173–4180
39 Liu Y Y, Montenbruck J M, Zelazo D, et al. A distributed control approach to formation balancing and maneuvering of multiple multirotor UAVs. IEEE Trans Robot, 2018, 34: 870–882
40 Luis C E, Schoellig A P. Trajectory generation for multiagent point-to-point transitions via distributed model predictive control. IEEE Robot Autom Lett, 2019, 4: 375–382
41 Arul S H, Manocha D. DCAD: decentralized collision avoidance with dynamics constraints for agile quadrotor swarms. IEEE Robot Autom Lett, 2020, 5: 1191–1198
42 Xue Q, Duan H B. Robust attitude control for reusable launch vehicles based on fractional calculus and pigeon-inspired optimization. IEEE CAA J Autom Sin, 2017, 4: 89–97
43 Yuan G S, Xia J, Duan H B. A continuous modeling method via improved pigeon-inspired optimization for wake vortices in UAVs close formation flight. Aerospace Sci Tech, 2022, 120: 107259
44 Yu Y P, Liu J C, Wei C. Hawk and pigeon's intelligence for UAV swarm dynamic combat game via competitive learning pigeon-inspired optimization. Sci China Tech Sci, 2022, 65: 1072–1086
45 Duan H B, Yang Z Y. Large civil aircraft receding horizon control based on Cauthy mutation pigeon inspired optimization (in Chinese). Sci Sin Tech, 2018, 48: 277–288
46 Bai T T, Wang D B, Masood R J. Formation control of quad-rotor UAV via PIO. Sci China Technol Sci, 2022, 65: 432–439
47 Qiu H X, Duan H B. A multi-objective pigeon-inspired optimization approach to UAV distributed flocking among obstacles. Inf Sci, 2018, 509: 515–529
48 Ruan W Y, Duan H B. Multi-UAV obstacle avoidance control via multi-objective social learning pigeon-inspired optimization. Front Inform Technol Electron Eng, 2020, 21: 740–748
49 Feng Q, Hai X S, Sun B, et al. Resilience optimization for multi-UAV formation reconfiguration via enhanced pigeon-inspired optimization. Chin J Aeronautics, 2022, 35: 110–123
50 Qi J T, Guo J J, Wang M M, et al. Formation tracking and obstacle avoidance for multiple quadrotors with static and dynamic Obstacles. IEEE Robot Autom Lett, 2022, 7: 1713–1720
51 Teixeira M A S, Neves-Jr F, Koubaa A, et al. A quadral-fuzzy control approach to flight formation by a fleet of unmanned aerial vehicles. IEEE Access, 2020, 8: 64366–64381
52 Seo J, Kim Y, Kim S, et al. Collision avoidance strategies for unmanned aerial vehicles in formation flight. IEEE Trans Aerosp Electron Syst, 2017, 53: 2718–2734
53 Pan Z H, Zhang C X, Xia Y Q, et al. An improved artificial potential field method for path planning and formation control of the multi-UAV systems. IEEE Trans Circuits Syst II, 2022, 69: 1129–1133
54 Zhao H B, Wen Y M, Wu S T, et al. Dynamic evaluation strategies for multiple aircrafts formation using collision and matching probabilities. IEEE CAA J Autom Sin, 2021, 8: 890–904
55 Aggravi M, Pacchierotti C, Giordano P R. Connectivity-maintenance teleoperation of a UAV fleet with wearable haptic feedback. IEEE Trans Automat Sci Eng, 2021, 18: 1243–1262
56 Fernandes P B, Oliveira R C L, Neto J V F. Trajectory planning of autonomous mobile robots applying a particle swarm optimization algorithm with peaks of diversity. Appl Soft Comput, 2022, 116: 108108